Icarus 378 (2022) 114921

Contents lists available at ScienceDirect

Icarus

journal homepage: www.elsevier.com/locate/icarus

Spectral effects of regolith porosity in the mid-IR – Forsteritic olivine

A.C. Martin [a,*], J.P. Emery [a], M.J. Loeffler [a,b]

[a] Department of Astronomy and Planetary Science, Northern Arizona University, Flagstaff, AZ 86011, United States of America
[b] Center for Materials Interfaces in Research and Applications, Northern Arizona University, Flagstaff, AZ 86011, United States of America

ARTICLE INFO

Keywords:
Experimental techniques
Infrared observations
Regoliths
Spectroscopy
Trojan asteroids

ABSTRACT

Studies have long utilized laboratory derived spectra to understand the surface composition and other properties of planetary bodies. One variable that is believed to affect remotely acquired spectra in the mid-infrared (MIR; 5–35 μm) is the surface porosity of the airless body, yet there have been few laboratory studies to quantify this effect. Thus, here we report systematic laboratory experiments aimed at quantifying the effect that porosity has on the MIR spectra of silicate regoliths. To simulate the effects of regolith porosity, we mixed olivine powder with KBr powder of the same size range (< 20 μm, 20–45 μm, and 45–63 μm). Olivine was mixed with KBr from 0% - 90% with 10% intervals by weight. Finally, we measured spectra with a Fourier transform infrared (FTIR) spectrometer in the MIR. Our results indicate a transition from a primarily surface scattering regime to a primarily volume scattering regime with increasing regolith porosity. Evidence of the dominating regime transition includes: the primary Christiansen Feature at ~8.8 μm decreases in spectral contrast, and shifts slightly to longer wavelengths as regolith porosity increases, reststrahlen bands in the 10-μm region do not shift significantly in wavelength but do decrease in spectral contrast, vibrational bands in the volume scattering regime (i.e., peaks in emissivity) increase in spectral contrast with increasing regolith porosity, and the spectral contrast of 10-μm plateau increases exponentially with increasing regolith porosity. The MIR spectral analysis of asteroids, such as Hektor, suggests a highly porous surface regolith (at least 81% void space) of fine-particulate silicates. These results demonstrate that some asteroids support highly porous regoliths whose spectra are not well-matched by standard (low porosity) laboratory spectra of powders. The spectra presented here enable analysis of both the porosity and mineralogy of olivine-rich, low porosity asteroid surfaces.

1. Introduction

In an effort to understand the surface properties of planetary bodies, laboratory studies of analog surfaces have been utilized for decades. Libraries of various minerals and rocks with widely ranging compositions, particle sizes, and other variables have been developed for remote sensing applications of visible and near-infrared (VNIR; 0.5–2.5 μm) spectra (e.g., REflectance Experiment LABoratory, known as RELAB). Additional libraries (e.g., German Aerospace Center's Berlin Emissivity Database, known as DLR-BED, and the Arizona State spectral library), and specific investigations (e.g., Lane et al., 2011) that extend into the mid-infrared (MIR; 5–35 μm) offer the opportunity to extract additional information out of a given spectrum. The MIR is extremely useful for a myriad of analyses due to the complexity of entwined variables such as composition, particle size, and temperature. This complexity makes analog comparisons to planetary surfaces challenging.

Laboratory studies from the 1960s to the 1990s laid the groundwork for the understanding and application of MIR spectra for mineral identification via remote sensing. Very large absorption coefficients at the centers of Si—O stretching and bending vibrational modes in silicates and rapidly changing (as a function of wavelength) absorption coefficients on the wings of these bands lead to complex dependences on particle size and packing state of granular materials (e.g., Spitzer and Kleinman, 1961; Vincent and Hunt, 1968; Salisbury and Wald, 1992; Mustard and Hays, 1997; Lane, 1999). Large particles and closely packed regoliths show a strong contribution from surface scattering in the region around the center of strong molecular vibration bands, where absorption coefficients are large. In this scattering regime, the features appear as emissivity minima, called restrahlen bands, and the center is shifted to shorter wavelengths from the true vibrational band center. As particle size decreases (and as particles become more separated) volume scattering is introduced. When a given band is in the volume scattering regime, it appears as a peak rather than a minimum, and the center of the peak is at the vibrational band center (e.g., Vincent and Hunt, 1968;

* Corresponding author.
E-mail address: acm586@nau.edu (A.C. Martin).

https://doi.org/10.1016/j.icarus.2022.114921
Received 9 July 2021; Received in revised form 5 January 2022; Accepted 30 January 2022
Available online 7 February 2022

Hunt and Logan, 1972; Moersch and Christensen, 1995; Lane, 1999; Hapke, 2012). When volume scattering dominates the entire spectrum (e.g., for very fine and/or dispersed particles), all fundamental bands appear as peaks rather than minima, as commonly observed in spectra of comet comae (e.g., Harker, 2002; Lisse et al., 2006). In addition, as particle size decreases, the 10-μm region reststrahlen bands (RBs) exhibit a decrease in spectral contrast and feature broadening, but band positions do not change (Mustard and Hays, 1997; Lane and Christensen, 1998). Transparency features are attributed to low absorption coefficients that lead to an increased number of photon interactions (Salisbury and Walter, 1989; Salisbury and Wald, 1992), and in spectra of olivine (OLV) particles, the 13 μm transparency feature shifts toward shorter wavelengths and exhibits increasingly asymmetric behaviors with a decrease in particle size (Mustard and Hays, 1997).

Laboratory studies have shown that MIR spectra are also affected by silicate composition. For example, OLV band positions in the MIR increase in wavelength approximately linearly with increasing Fe content (e.g., Koike et al., 2003; Hofmeister and Pitman, 2007; Hamilton, 2010; Lane et al., 2011), with the minor exception of a small slope change near Fe_{70} (Hamilton, 2010). Koike et al. (2003), and Lane et al. (2011) also show that the position of fundamental Si—O vibrational bands in OLV shift linearly with increasing Fe content (e.g., the forsterite band at 10.06 μm (994 cm^{-1}) shifts to 10.51 μm (951 cm^{-1}), as iron substitutes into the structure and the composition becomes fayalite). The large absorption coefficients are associated with stretching and bending of Si—O bonds, and cations (i.e., Fe and Mg) that have different properties, such as radius and mass, affect the bond's vibrational frequency and subsequently the band position (e.g., Koike et al., 2003; Hamilton, 2010). The sensitivity to composition as well as particle size on silicate features in the MIR (e.g., Logan et al., 1973; Koike et al., 2010), make this spectral region challenging, yet ideal for assessing the silicate mineralogy and regolith particle size and porosity on asteroids.

The surface spectra of Jupiter's Trojan asteroids (hereafter Trojans) represent prime examples of this challenge. MIR spectra of three Trojans (624 Hektor, 1172 Aneas, and 911 Agamemnon) taken with the Spitzer Space Telescope reveal broad 10-μm emissivity features that look similar to Jupiter family comet (JFC) comae, such as Hale-Bopp and Schwassmann-Wachmann 1 (Fig. 1; Emery et al., 2006). Cometary comae are generally optically thin, resulting in a broad 10-μm plateau of muted fundamental silicate bands (~9.5 μm to 13 μm) bounded by deep transparency-related lower-emissivity regions (e.g., Harker et al. 2002, Lisse et al., 2006). Trojans do not have comae (e.g., Perna et al., 2018), so the presence of comet-like features was unexpected. Other primitive asteroids such as (87) Sylvia, and (762) Pulcova as well as the nucleus of comets 9P/Tempel 1 and 49P/Arend-Rigaux show similar emissivity features (Marchis et al., 2012; Kelley et al., 2017).

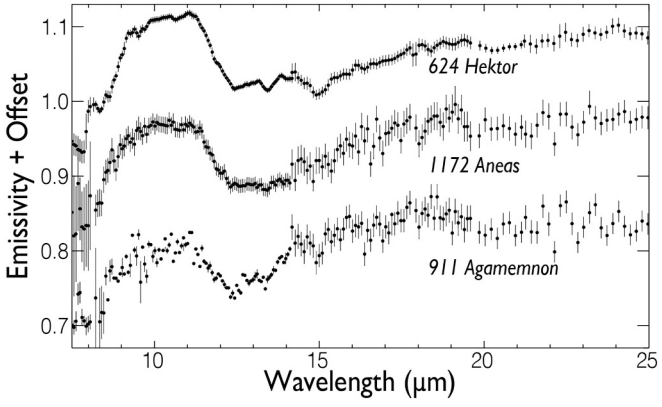

Fig. 1. Thermal infrared spectra of Trojan asteroids Hektor, Aneas, and Agamemnon.
Modified from Emery et al. (2006).

It has not been possible to fully interpret MIR spectra of Trojan asteroids with existing laboratory data and modeling. Typically, MIR spectra of regoliths exhibit emissivity minima near 10 and 20 μm, due to anomalous surface scattering (i.e., extremely strong absorption coefficients) in the Si—O fundamental vibrational bands (e.g., Christensen et al., 2000; Donaldson-Hanna et al., 2017). Emery et al. (2006) noted Trojan and comet comae spectra exhibit emissivity *peaks* at these wavelengths, indicating a configuration where surface scattering is small and primary emission is dominant (e.g., Hunt and Logan, 1972). The leading theories to explain the Trojan spectra suggest that observed emissivity peaks may arise from a fluffy regolith of fine particulate silicates, or from silicates suspended in a transparent matrix (Emery et al., 2006; Vernazza et al., 2012; Yang et al., 2013). In either case, the MIR spectra indicate that the surfaces of Hektor, Aneas, and Agamemnon contain fine particulate silicates.

Properly characterizing the surface composition of asteroids provides insight into where they formed, as Mg-rich crystalline silicates tended to form in the inner Solar System, and Fe-rich silicates formed in the outer Solar System (Gail, 2004; Henning, 2010). Calibration of methods to determine the Mg# (i.e., Mg/(Mg + Fe)) of silicates from remote sensing spectra is critical for interpreting possible formation regions. OLV is commonly found throughout the Solar System, it appears as a dominant phase in comet comae (e.g., Wooden et al., 2017), and it has been suggested to be qualitatively consistent with the MIR spectra of Trojans (Emery et al., 2006; Vernazza et al., 2015).

Vernazza et al. (2012) present results of mixtures of OLV- rich meteorites with potassium bromide (KBr), an IR-transparent salt, and compare the mixture spectra to the spectrum of Hektor. Their results indicate a KBr diluted sample is a better match to Hektor's MIR spectrum than are spectra of pure powdered silicates, indicating Trojans have a porous or salty regolith dominated by volume scattering throughout the MIR Si—O vibrational bands, which is consistent with previous studies (Emery et al., 2006; Yang and Jewitt, 2011). Young et al. (2019) looked at three to four degrees of regolith porosity with fine-particulate quartz and phyllosilicates mixed with KBr, as well as two to four degrees of darkening using two different darkening agents (nanophase iron oxide, and activated carbon). They found the primary Christiansen Feature (CF; emissivity maximum that occurs where a strong band transitions from volume scattering to surface scattering as teh real portion of teh refractive index increases) shifted, and the transparency feature (TF; a region of volume scattering between regions dominated by surface scattering), near 13 μm, broadened with the addition of simulated porosity (i.e., KBr). This simulated porosity provides a somewhat better match to Trojan spectra than samples that contain no KBr (Young et al., 2019). Izawa et al. (2021) studied the effect of meteorite powders mixed with KBr to investigate the feasibility of detecting salts from remote observations. They found that the addition of KBr increases the overall albedo and salt-meteorite spectra show some features weaken from low to high concentrations of KBr in a given sample, but KBr does not produce detectable features of its own.

Following on the previous work that demonstrates that MIR spectra of Trojan and other asteroid surfaces can be qualitatively explained by high regolith porosity, we performed systematic laboratory reflectance experiments aimed at quantifying the effect that porosity has on the MIR spectra of silicate regoliths. This study is the first of several focusing on other silicate minerals that are relevant to Trojan and other primitive asteroid surfaces. In this paper, we focus on olivine, which is highly relevant to Trojan asteroids, comet nuclei, and some main belt asteroids to name a few. We present results on spectral effects induced by varying porosity, particle size, and composition of olivine to identify which spectral features are altered most by increased porosity, and which are the best for identifying and determining the Mg# of olivine on asteroid surfaces. Finally, we place these results in the context of Trojan asteroids.

2. Methods

2.1. Sample suite

For these experiments, we purchased two natural forsteritic OLVs (OLV_1 and OLV_2) from Mineralogical Research Company with slightly different Mg#s. OLV_1 and OLV_2 were originally from the Canary Islands and San Carlos, AZ, respectively. Because our samples are natural, contamination from other mineral phases is not uncommon. Thus, to determine the mineralogy, silicate Mg#, and identify any potential contaminants, we performed petrologic analysis using a Cameca SX-100 Electron Microprobe (EMP) at the University of Tennessee.

We found that OLV_1 has an Mg# of 91.02 ± 0.20 with potential minor diopside, enstatite, spinel, and phyllosilicate phases and confirmed OLV_2 is a San Carlos OLV (Mg# of 90.10 ± 0.00) with no additional phases.

2.2. Sample preparation and measurement

To prepare the OLV samples, we separated the target silicates (OLV) from other phases using tweezers, ground them with an agate mortar and pestle, and sieved with a Gilson Performer III Sieve Shaker into three particle size ranges: < 20 μm, 20–45 μm, and 45–63 μm. Samples of the larger two particle sizes were rinsed to remove clinging fines. These particle size ranges were selected because surface scattering begins to give way to volume scattering for particle sizes around 65 μm, depending on the absorption coefficient (e.g., Hamilton, 2010). As volume scattering becomes increasingly important, the 10-μm region of the Si—O stretching band forms a plateau, and MIR spectra of Trojan asteroids exhibit this apparent inversion indicative of volume scattering from fine-particulate silicates (Emery et al., 2006). Additionally, thermal inertia measurements of Trojans suggest surfaces composed of fine-particulate material (e.g., Fernández et al., 2003; Mueller et al., 2010), and near-infrared (NIR;0.7–2.5 μm) spectral modeling of NIR spectra of 30 different Trojans is consistent, estimating particle sizes of ≲100 μm (Emery and Brown, 2004; Yang and Jewitt, 2011; Sharkey et al., 2019).

To simulate the effects of porosity, we mixed OLV powders with KBr powder ground and sieved into the same particle size ranges. The KBr size ranges were restricted to ensure homogeneous sample mixtures, as well as to reduce the potential effect of particle size sorting (also known as the 'brazil nut effect') that may occur when transporting the sample cups. KBr is transparent (i.e., has very low absorptivity) in the MIR, so it is used as a proxy for porosity. KBr, as opposed to other transparent material was chosen because it is relatively inexpensive, accessible, and commonly used in laboratory research (e.g., Vernazza et al., 2012). Each OLV powder sample is then mixed with KBr in ratios from 0% to 90% by weight, in 10 wt% intervals, to simulate differing levels of porosity (Table 1). To be consistent with previous studies (e.g., King et al., 2011; Izawa et al., 2021), we use the term 'regolith porosity' to refer to the wt % of KBr in a sample. Uncertainties in the wt% are dominated by the precision of the balance (1 mg) and are <0.5%. The sample cups were tapped as they were filled with OLV + KBr mixtures to promote even particle dispersal. The sample cup tops were leveled by scraping using a straight edge razor, while being careful to not compress the powdered mixtures in the process.

While the regolith porosity term is used to be consistent with previous studies, we point out that there is additional empty space in the sample cup we call 'sample cup porosity' (V_{air}). V_{air} is the vol% of air in the sample cup that fills the space in-between OLV and KBr particles. The more comparable value to the porosity on an asteroid surface is the volume taken up by KBr (V_{KBr}) and V_{air} taken together. We call this quantity 'total simulated porosity', and it is given by $(V_{KBr} + V_{air})/V_{SC}$. The sample cup volume (V_{SC}) was determined as the difference in weight between the sample cup when filled with liquid water and when empty, divided by the density of water (1 g/cm^3). The result is consistent with equipment specifications from the manufacturer (Pike Technologies macro sample cup; 0.181 cm^3). The fraction of porosity due to air is computed from

$$Porosity_{air} = 1 - \frac{V_{Sample}}{V_{SC}}, \quad (1)$$

where the total volume of each sample (V_{Sample}) was determined by weighing the difference between an empty sample cup and one filled with the sample, and dividing by the corresponding bulk density for a given mineral (e.g., forsterite: 3.27 g/cm^3, and KBr: 2.75 g/cm^3). The V_{KBr} term is computed by multiplying the wt% KBr [$f_{KBr} = m_{KBr}/(m_{KBr} + m_{mineral})$] by the measured mass of the sample and dividing by the density of KBr:

Table 1
The weight percent of KBr in a sample (Regolith Porosity; units in wt%), the percent volumetric contribution of air to the empty space in a sample cup (Sample Cup Porosity; units in vol%), and the combined percent volumetric contribution of air and KBr in a sample cup (Total Simulated Porosity; units in vol%) are listed above for each sample in all three particle size bins.

	Regolith porosity (wt% KBr)			Sample cup porosity (vol% air)			Total simulated porosity (vol% air + KBr)		
	<20 μm	20–45 μm	45–63 μm	<20 μm	20–45 μm	45–63 μm	<20 μm	20–45 μm	45–63 μm
$OLV_{1,100}$	0.00	0.00	0.00	59.71	57.17	55.65	59.71	57.17	55.65
$OLV_{1,\ 90}$	10.50	11.94	10.10	71.87	57.56	53.48	75.15	63.33	59.67
$OLV_{1,\ 80}$	18.91	19.59	20.13	71.06	58.89	51.42	77.62	68.56	62.95
$OLV_{1,\ 70}$	29.08	29.43	29.90	70.62	58.88	55.95	80.67	73.00	70.45
$OLV_{1,\ 60}$	39.41	39.13	39.67	65.65	61.35	56.01	80.82	78.88	75.38
$OLV_{1,\ 50}$	47.50	48.78	50.00	66.54	62.99	53.68	84.71	83.09	78.84
$OLV_{1,\ 40}$	59.70	60.33	60.07	68.62	61.12	56.71	88.74	85.63	84.52
$OLV_{1,\ 30}$	69.00	68.95	71.08	67.39	59.91	60.46	91.24	89.17	89.82
$OLV_{1,\ 20}$	80.00	79.21	79.02	68.07	63.74	57.43	94.51	93.52	92.32
$OLV_{1,\ 10}$	90.05	88.35	88.41	66.90	65.13	56.07	97.17	96.51	95.70
$OLV_{2,100}$	0.00	0.00	0.00	68.90	55.65	52.26	68.90	55.65	52.26
$OLV_{2,\ 90}$	10.45	11.33	10.34	69.44	63.86	51.07	73.17	68.63	56.97
$OLV_{2,\ 80}$	20.40	20.79	20.49	69.06	62.52	52.25	76.28	71.44	63.45
$OLV_{2,\ 70}$	30.20	30.73	30.88	70.83	64.89	44.19	80.74	77.02	63.56
$OLV_{2,\ 60}$	39.80	40.20	40.39	70.69	61.75	49.07	83.59	78.74	71.79
$OLV_{2,\ 50}$	50.50	49.50	50.00	67.36	63.34	46.73	85.25	83.07	75.66
$OLV_{2,\ 40}$	60.00	60.40	59.90	68.33	63.41	39.80	88.62	86.99	78.31
$OLV_{2,\ 30}$	69.65	69.61	69.12	68.00	62.07	44.20	91.42	89.81	84.76
$OLV_{2,\ 20}$	79.21	80.00	80.10	69.05	62.38	49.41	94.40	93.47	91.26
$OLV_{2,\ 10}$	89.11	89.55	89.60	72.50	61.79	53.36	97.44	96.59	95.85

$$V_{KBr} = \frac{f_{KBr}(m_{KBr} + m_{mineral})}{\rho_{KBr}}. \quad (2)$$

The contribution to porosity from KBr is computed from Eq. (1), exchanging V_{KBr} for V_{sample}. The porosity due to air and due to KBr are then added to get the total simulated porosity. Masses were measured several times to assess the uncertainty for the total simulated porosity estimates (Table 1).

Following the porosity calculations, MIR reflectance measurements of OLV_1 were taken with an Agilent Cary 600 Series Fourier transform infrared (FTIR), and OLV_2 measurements were taken with a Thermo-Nicolet IS50 Fourier transform infrared (FTIR) spectrometer, both under ambient temperature and pressure conditions. Two different spectrometers were used due to instrument availability; we measured a few samples with both spectrometers to verify they produced identical spectra (within measurement noise). The PIKE Technologies EasiDiff diffuse reflectance accessory was utilized in both cases and the reflected intensity (I) was an average of 200 scans between 4000 and 400 cm^{-1} at a 4 cm^{-1} spectral sampling. For each OLV mixture, we averaged the reflected intensity (I_s) of two or more separate sample spectra. In between sample spectra, we measured the reflected intensity of pure KBr powder (I_{ref}) using the same particle size range as the target OLV mixture. The resulting reflectance spectrum (R) is I_s / I_{ref}.

Laboratory reflectance (R) measurements were converted to emissivity (E), using Kirchhoff's law (E = 1 – R). Although Kirchhoff's law is only strictly valid in an absolute sense for hemispherical reflectance, in practice, applying it to diffuse reflectance, as we measure, does not affect significantly band positions, shapes, or relative strengths (e.g., Salisbury et al., 1991; Salisbury et al., 1994; Vernazza et al., 2012; Young et al., 2019).

3. Results

3.1. OLV_1

The MIR spectra of the 100% OLV_1 sample with different particle sizes have strong resemblances to one another (Fig. 2). For an agnostic analysis, we identify peaks (P) and dips (D) in the spectra. These peaks and dips do not *necessarily* correspond to reststrahlen or vibrational bands; rather, their position, width, and spectral contrast are used to describe different spectral shapes, and compare spectra in different scattering regimes to each other (described in more detail in the analysis, Section 4.1). Commonalities among the spectra of 100% OLV_1 include a strong peak present at ~9.0 μm (P_2) that corresponds to the primary Christiansen Feature (CF_1), a shoulder at slightly longer wavelengths where the emission dips and then rises sharply to form the left side of a narrow (~0.5 μm wide) plateau. This plateau has a sharp feature on the long wavelength side near ~10.0 μm (P_4). At longer wavelengths, the spectra exhibit a double-peak emission (P_8 near 11.6 μm and P_9 near 11.9 μm), then steeply dive into the transparency feature (TF; D_7) that bottoms out at ~13 μm. An additional double peak at

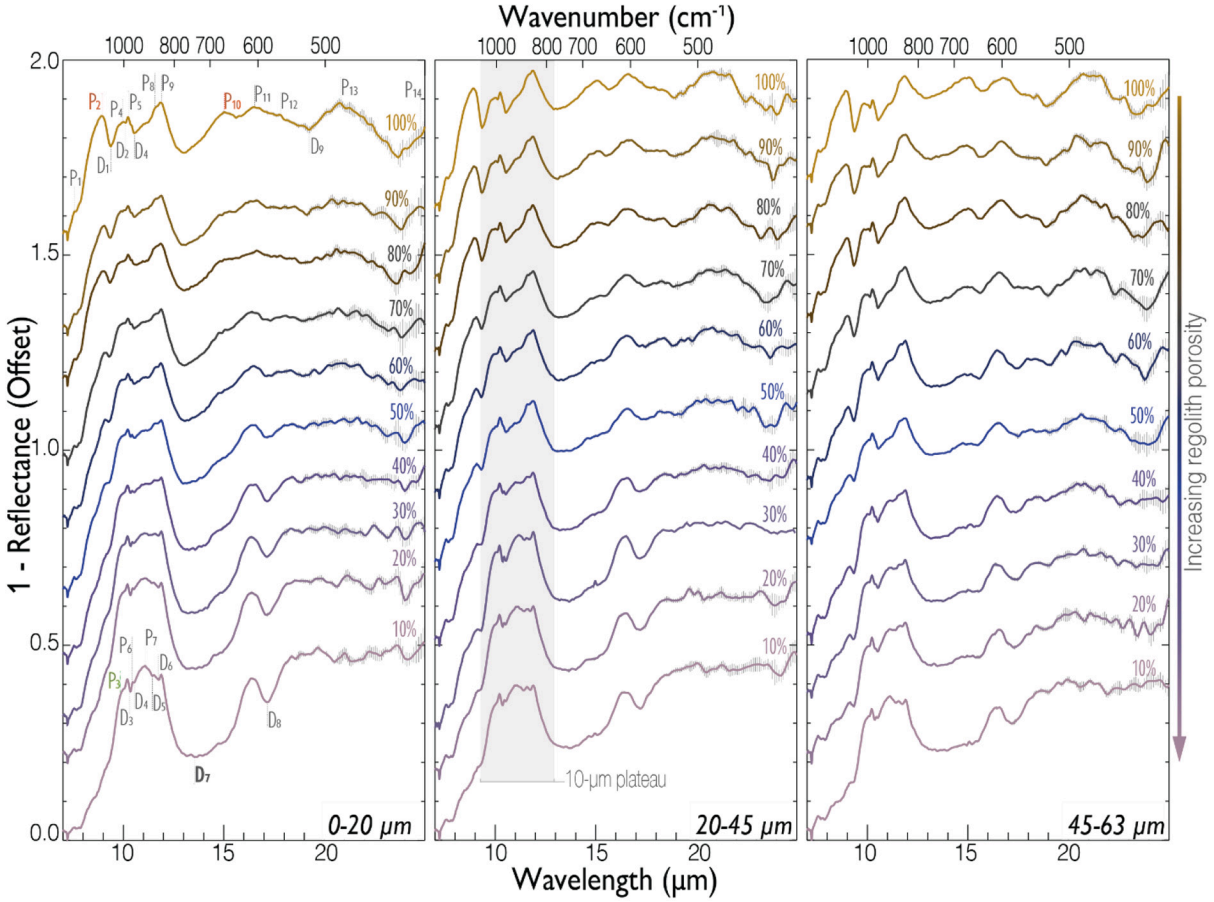

Fig. 2. Spectra of OLV_1 powder mixed with increasing wt% of KBr (from top to bottom) to represent regolith porosity. Measurement uncertainties are shown with gray bars (most apparent at the longest wavelengths). Percentages listed for each spectra represent the weight percent of OLV_1. Each panel contains a different range of particle sizes (from left to right: 0–20, 20–45, and 45–63 μm). Spectra have been vertically offset for clarity and features are labeled in the 0–20 μm panel. The 0–20 μm spectral plot, shows peaks labeled with 'P', and dips labeled with 'D'. The shoulder (P_3) is labeled in green; the two CFs (P_2 and P_{10}) are labeled in red; the transparency feature (D_7) label is bolded. The approximate 10-μm plateau region is shaded slightly in the 20–45 μm spectral plot. (For interpretation of the references to colour in this figure legend, the reader is referred to the web version of this article.)

~16.5 (P_{11}) and 18.3 μm (P_{12}), as well as a single feature at ~21.1 μm (P_{13}) are also apparent in all particle sizes studied.

The characteristics of OLV_1 spectra mentioned above change significantly with increasing KBr fraction (i.e., regolith porosity; Fig. 2). The spectral contrast (generally defined as is the height of the feature above the feature continuum; see Section 4.1.1) of CF_1 (P_2) decreases from 15% to 0% as the porosity increases. The shoulder (P_3 - defined in Section 4.2.1.1) on the narrow plateau at ~9.8 μm remains the same, as does the overall shape of P_4, and P_5. A small dip (D_4) shallows, and eventually a broad plateau forms (~5.3 μm wide for 10% OLV_1 at the base) for spectra of samples with ≲40% OLV_1 by weight or less. The plateau is defined by the shoulder (P_3) on the short wavelength side and P_9 on the long wavelength side. A prominent emission peak (P_7) develops in the center of the broad plateau and increases in spectral contrast with increasing regolith porosity. The TF region widens, and CF_2 (the secondary CF; P_{10}) decreases in spectral contrast, while P_{11} becomes more distinct. The clear peak of P_{13} observed in 100% OLV_1 decreases with increasing regolith porosity until it is below the noise level.

3.2. OLV_2

The MIR spectra of the 100% OLV_2 sample for the two larger particle sizes have strong resemblances to each other, but have a few key differences compared to the <20 μm OLV_2 and all 100% OLV_1 spectra (Fig. 3). As was done with OLV_1 spectra, we identify emission peaks (P) and dips (D), which do not necessarily correspond to RBs or vibrational bands. The TF depth in the 20–45 μm and 45–63 μm 100% OLV_2 spectrum is quite shallow, and seems to mask P_8 and P_9. Additionally, features in the 10-μm region (e.g., P_3, P_4 for the 100% OLV_2 spectra in the two larger particle size samples) have much lower emissivity than P_2 (the CF_1). The <20 μm spectrum, however, is qualitatively similar to the OLV_1 spectra. Aside from these differences, the 100% OLV_2 spectra are quite similar to one another, regardless of particle size. Commonalities include a strong emission peak present at ~9 μm (P_2) that corresponds to the CF_1, and a shoulder (P_3) at slightly longer wavelengths where the emission dips and then rises sharply to form the left side of a narrow (~0.5 μm wide) plateau. This plateau has a sharp feature on the long wavelength side at ~11.9 μm (P_9). Additional peaks at ~16.6 (P_{11}), 18.4 μm (P_{12}), and ~ 20.7 μm (P_{13}) are also apparent in the two samples with the smallest particle sizes.

The characteristics of the 100% OLV_2 spectra mentioned above are altered as KBr is incorporated into the mixture. However, the changes show different dependences (described in more detail in 4.1.2) than what was observed in the OLV_1 samples. The feature with the largest change in spectral contrast is the CF_1 (P_2), which decreases from ~20% to 0%. The shoulder on the narrow plateau remains in the same position (at ~9.8 μm), as does the overall shape of P_4 (with the exception of the 100% OLV_2 samples). A small dip (D_2) to the long wavelength side of P_4 shallows, and eventually forms a broad plateau (~5.1 μm wide at the base for <20 μm 10% OLV_2 spectrum) marked by the shoulder on the short wavelength side and P_9 on the long wavelength side. A prominent emission peak develops and increases in spectral contrast with increasing regolith porosity in the center of the broad plateau (P_7). The TF region widens and deepens, and P_{10} (CF_2) decreases in spectral contrast while P_{11} becomes more distinct. P_{13} observed in 100% OLV_2 spectrum shallows and eventually looks inverted with increasing regolith porosity.

4. Analysis

In this section we outline the feature parameters that we used to quantify how our spectra change regolith porosity. In this analysis, we distinguish the feature parameters of 'individual features' and those of the 10-μm plateau. For the analysis to remain agnostic, we report the feature parameters that are dependent on regolith porosity, as well as trends that are not. In this way, we hope to elucidate feature parameters that are most useful to consider when analyzing remote sensing data. Applicability of laboratory data to remote observations is described in detail in Discussion Section 5.4.

4.1. Individual features

4.1.1. Feature parameter assignments

After converting FTIR spectra into emissivity, we began analysis by identifying silicate features and quantifying their positions with an Interactive Data Language (IDL) feature finding routine, developed for this project, that searches for local maxima and minima iteratively across a spectrum. Feature positions for a given mineral's particle size range were identified in each mineral mixture spectrum to determine if there is a shift associated with porosity, and if that shift is dependent on particle size and/or mineralogy. We additionally characterized the feature parameters of each silicate feature for each porosity step. We are particularly interested in the fundamental vibrational features, which are most diagnostic for OLV identification (e.g., Hamilton, 2000; Chihara et al., 2002; Koike et al., 2003; Hofmeister and Pitman, 2007; Lane et al., 2011).

In order to locate these emissivity features (i.e., peaks and dips), the spectrum is first smoothed with a Gaussian kernel to reduce noise. The smoothing window for OLV_1 and OLV_2 was set from 5 to 15 spectral channels (or data points). This value can be altered based on the level of noise of a given spectrum. Once smoothed, we take the derivative of our spectrum using the IDL function '*deriv*', which uses three-point (quadratic) Lagrangian interpolation to compute the derivative. Next, potential features are identified as local minima or local maxima. Then, the slope of the feature is determined and checked against a user provided minimum slope to rule out possible noise. Once a potential feature is identified, we take a small segment of the spectrum on either side of the feature and find the wavelength of the maximum or minimum value, for a peak or dip, respectively, within that subgroup. This process avoids collecting peaks/dips clearly caused by noise, while still retrieving narrow and broad peaks in a given spectrum. For a spectrum with negligible noise the slope check and spectral bracketing would not be necessary (i.e., finding where the first derivative is zero would suffice), but because there is noise, these additional steps are needed. We identified 14 peaks (labeled P#) and 9 dips (labeled D#) with our IDL fitting routine.

The aforementioned routine provides the feature positions (x,y), and the following steps are used to identify the remaining feature parameters. The edges of each identified peak are defined by the adjacent dips. The line between these edges is the local continuum, and the distance between the edges is the base width. Spectral contrast is the height of the feature above the feature continuum and is given by an equation from Clark and Roush (1984) applied to emissivity,

$$(E_{max} - E_{cont})/E_{cont}, \quad (3)$$

where E_{max} is the emissivity at the band maximum and E_{cont} is the emissivity of the continuum at the same wavelength. This definition of spectral contrast is consistent with VNIR and MIR laboratory spectral analysis for planetary remote sensing applications (e.g., Hamilton et al., 2008). The feature's y-position is used to calculate the full width at half max (FWHM). Finally, the area is calculated by integrating the area between the continuum and spectrum of each feature. Features, especially in the 10-μm region, may consist of multiple overlapping bands, potentially complicating our measurements. Thus, we assume we are in a scattering regime in which emission features are linearly additive, and as such, individual features are superposed onto the broad 10-μm plateau.

To estimate the feature parameter error, 10,000 synthetic versions of each feature segment are generated by randomly assigning values at each wavelength within the bounds of the spectral error bars, which

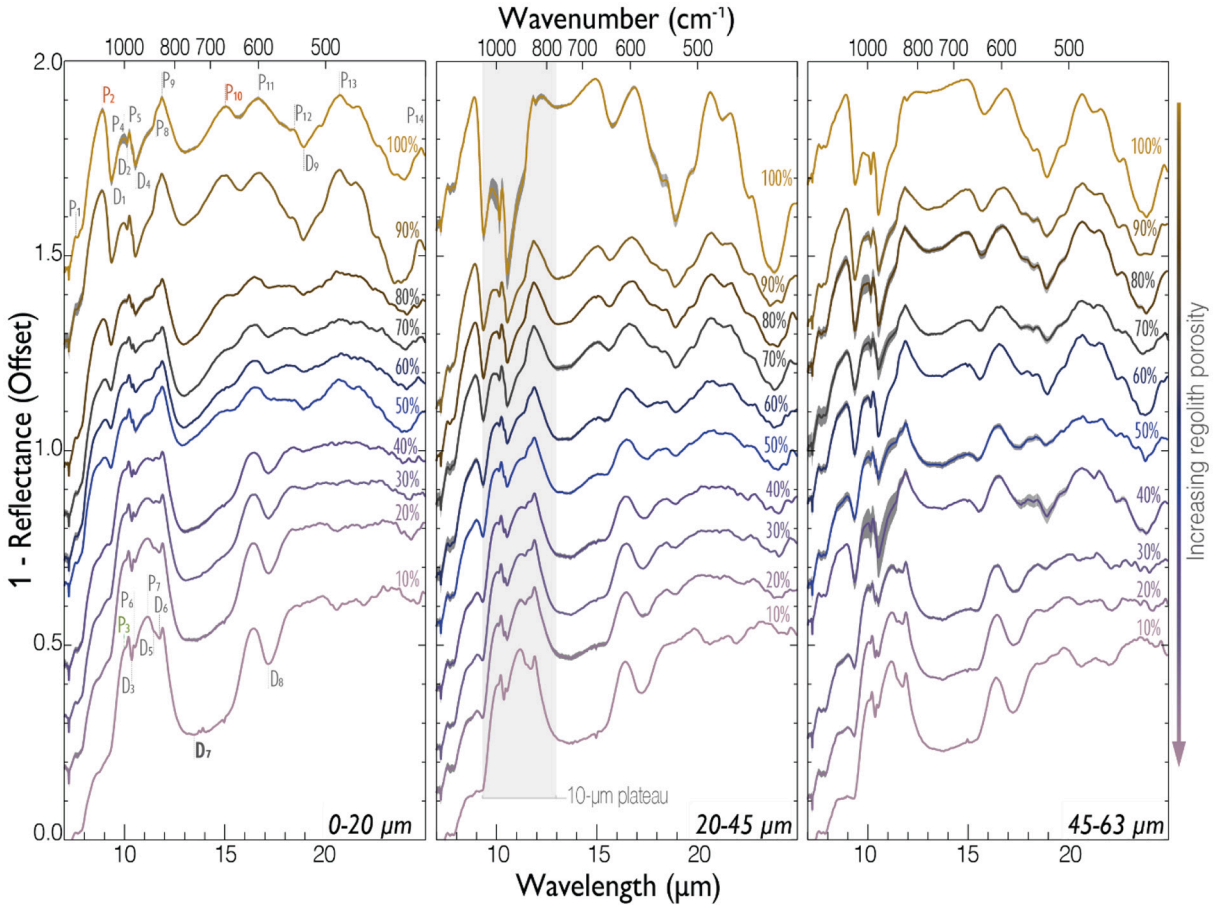

Fig. 3. Spectra of OLV_2 powder mixed with increasing wt% of KBr (from top to bottom) to represent regolith porosity. Measurement uncertainties are shown with gray bars (most apparent at the longest wavelengths). Percentages listed for each spectra represent the weight percent of OLV_1. Each panel contains a different range of particle sizes (from left to right: 0–20, 20–45, and 45–63 μm). Spectra have been vertically offset for clarity and features are labeled in the 0–20 μm panel. The 0–20 μm spectral plot, shows peaks labeled with 'P', and dips labeled with 'D'. The shoulder (P_3) is labeled in green; the two CFs (P_2 and P_{10}) are labeled in red; the transparency feature (D_7) label is bolded. The approximate 10-μm plateau region is shaded slightly in the 20–45 μm spectral plot. (For interpretation of the references to colour in this figure legend, the reader is referred to the web version of this article.)

were obtained by repeated measurements of the sample. Every synthetic spectrum is then fitted with a 4th order smoothing spline polynomial for feature parameter calculations. From the 10,000 synthetic segments, the means and standard deviations of the feature positions, width, FWHM, spectral contrast, and area are calculated.

4.1.2. Feature parameter trends

4.1.2.1. OLV_1. Individual peaks and dips as a function of regolith porosity are given in Tables 2 and 3. Many peak and dip positions do not change with increasing regolith porosity (defined as the ratio of OLV to KBr within a given sample cup) of a given sample (Fig. 4). Two of the exceptions are CF_1 (P_2) and CF_2 (P_{10}). CF_1 shifts to longer wavelengths by 0.195, 0.217 and 0.217 μm, and CF_2 shifts to shorter wavelengths by 0.595, 0.620, and 0.400 μm for the 0–20 μm, 20–45 μm and 45–63 μm spectra respectively. Other features that shift are found at the longest wavelengths, like P_{13} that shifts 0.911 μm to longer wavelengths for the 45–63 μm spectra. Features at these longer wavelengths are much broader, and therefore have larger uncertainties, but shifts in position are reliable. Dips that correspond to RBs and can be used for Mg# identification when regolith porosity is low, such as D_5, shift to longer wavelengths with increasing regolith porosity, and D_8 and D_9 shift to slightly shorter wavelengths. However, there are features frequently used for Mg# analysis, such as peaks P_5 and P_9, and the RB dips D_2 and D_4 (depending on the scattering regime), that do not shift significantly (see Section 5.2).

Characteristics that are affected by regolith porosity are spectral contrast, width, FWHM, and area of some peaks and some dips (see supplemental materials for parameter values). With decreasing regolith porosity, the spectral contrast decreases linearly for P_1, P_6, P_7, P_9, P_{11}, P_{12}, D_6, and D_7 for each particle size studied, and P_2, P_{10}, P_{13}, D_1, and D_4 increase in spectral contrast (Fig. 5). In fact, as the regolith porosity increases, some features appear (e.g., P_7) while others disappear (e.g, P_2). P_{10} (CF_2) almost goes to zero, but it does remain present throughout the spectral suite. At higher regolith porosities P_{10} is harder to identify, and thus the uncertainties associated with its band parameters are higher compared to other features. The FWHM increases with decreasing regolith porosity for P_2, P_5, P_{10}, P_{11}, D_1, D_2, D_4 and D_9, while the FWHM decreases for P_6, P_7, possibly P_{12} and P_{14} (although the error associated with P_{12} and P_{14} is very high), D_3, D_7, and D_8. P_2, P_4, P_5, P_{10}, P_{11}, D_1, D_2, D_4, D_5, and possibly D_9 get wider with increasing regolith porosity, whereas P_1, P_7, D_3, D_6, possibly D_7, and D_8 become narrower. Finally, the area of P_7, P_{11}, D_6, and D_7, increases with increasing regolith porosity, and the area of P_2, P_{10}, P_{12}, D_1, D_5, and D_9 decreases with increasing regolith porosity.

All feature parameters were also explored as a function of the other feature parameters (e.g., spectral contrast vs. feature position). Some weak relationships may be present; however, we do not find them significant. All feature parameter data tables can be found in the supplementary materials.

Table 2
The position of each peak feature for the OLV_1 spectral series. A small plus sign (+) indicates provisional fundamental vibrational bands when volume scattering dominates.

	Peak Position (μm) for the 0-20 μm samples													
	1	**2 (CF_1)**	**3 (sh)**	**4**	**5**	**6^+**	**7^+**	**8**	**9^+**	**10 (CF_2)**	**11^+**	**12**	**13**	**14**
$OLV_{1,100}$	7.596 ± 0.005	8.909 ± 0.016	9.749 ± 0.005	10.032 ± 0.014	10.238 ± 0.012		10.986	11.600 ± 0.006	11.853 ± 0.023	15.077 ± 0.044	16.499 ± 0.046		20.865 ± 0.247	
$OLV_{1,90}$	7.561 ± 0.008	9.055 ± 0.017	9.766 ± 0.001	10.077 ± 0.027	10.228 ± 0.015		10.94	11.589 ± 0.013	11.890 ± 0.014	14.754 ± 0.031	16.532 ± 0.093	18.434 ± 0.106	21.410 ± 0.695	23.109 ± 0.140
$OLV_{1,80}$	7.586 ± 0.007	9.024 ± 0.034	9.736 ± 0.009		10.238 ± 0.010		10.963	11.549 ± 0.001	11.862 ± 0.015	14.748 ± 0.066	16.659 ± 0.052	18.188 ± 0.464	21.369 ± 0.418	
$OLV_{1,70}$	7.568 ± 0.008	9.078 ± 0.039	9.766 ± 0.001		10.227 ± 0.001		10.917	11.562 ± 0.013	11.892 ± 0.001	14.688 ± 0.118	16.320 ± 0.070	18.380 ± 0.360	20.925 ± 0.381	
$OLV_{1,60}$	7.598 ± 0.085	9.104 ± 0.037	9.766 ± 0.001	10.040 ± 0.039	10.227 ± 0.001		10.956 ± 0.030	11.601 ± 0.001	11.857 ± 0.022	14.679 ± 0.061	16.467 ± 0.015	18.310 ± 0.102	21.689 ± 0.228	
$OLV_{1,50}$	7.560 ± 0.002		9.781 ± 0.006		10.228 ± 0.003	10.434 ± 0.006	10.908 ± 0.024	11.539 ± 0.018	11.894 ± 0.013	14.483 ± 0.119	16.483 ± 0.030	18.101 ± 0.096		
$OLV_{1,40}$	7.538 ± 0.008		9.783 ± 0.001		10.216 ± 0.010	10.442 ± 0.010	10.915 ± 0.017	11.527 ± 0.047	11.881 ± 0.014	14.547 ± 0.137	16.509 ± 0.076	18.144 ± 0.115		
$OLV_{1,30}$	7.564 ± 0.007		9.803 ± 0.001		10.209 ± 0.001	10.455 ± 0.008	10.961 ± 0.050	11.605 ± 0.065	11.902 ± 0.019	14.609 ± 0.164	16.347 ± 0.034	18.236 ± 0.131		
$OLV_{1,20}$	7.547 ± 0.016		9.803 ± 0.001		10.207 ± 0.005	10.461 ± 0.020	10.93 ± 0.056	11.560 ± 0.074	11.892 ± 0.001	14.495 ± 0.106	16.368 ± 0.078			
$OLV_{1,10}$	7.680 ± 0.112		9.801 ± 0.005		10.207 ± 0.006	10.478 ± 0.009	11.029 ± 0.047	11.552 ± 0.017	11.898 ± 0.016	14.655 ± 0.219	16.386 ± 0.028			
Δ (μm)	0.142	0.195	0.067	0.045	0.031	0.044	0.122	0.079	0.048	0.595	0.339	0.333	0.824	N/A
Slope	0.000	−0.004	−0.001	0.000	0.000	−0.001	0.000	0.000	0.000	0.004	0.002	0.003	−0.012	N/A
χ2	0.014	0.006	0.001	0.001	0.000	0.000	0.012	0.006	0.002	0.123	0.065	0.061	0.344	N/A
	Peak Position (μm) for the 20-45 μm samples													
	1	**2 (CF_1)**	**3 (sh)**	**4**	**5**	**6^+**	**7^+**	**8**	**9^+**	**10 (CF_2)**	**11^+**	**12**	**13**	**14**
$OLV_{1,100}$	7.575 ± 0.010	8.902 ± 0.009	9.766 ± 0.001	10.014 ± 0.025	10.249 ± 0.001		10.894	11.600 ± 0.006	11.867 ± 0.001	15.106 ± 0.046	16.589 ± 0.033	18.413 ± 0.111	20.950 ± 0.157	22.863 ± 0.103
$OLV_{1,90}$	7.570 ± 0.001	8.945 ± 0.015	9.765 ± 0.004	10.031 ± 0.001	10.236 ± 0.010		10.963	11.586 ± 0.013	11.868 ± 0.006	15.103 ± 0.043	16.730 ± 0.075	18.360 ± 0.274	20.755 ± 0.226	22.650 ± 0.120
$OLV_{1,80}$	7.565 ± 0.005	8.954 ± 0.032	9.781 ± 0.006	10.025 ± 0.017	10.240 ± 0.010		11.033	11.601 ± 0.001	11.868 ± 0.004	15.056 ± 0.152	16.649 ± 0.124	18.379 ± 0.045	20.973 ± 0.474	22.808 ± 0.092
$OLV_{1,70}$	7.576 ± 0.005	9.049 ± 0.003	9.773 ± 0.009	10.041 ± 0.020	10.236 ± 0.010		10.894	11.601 ± 0.001	11.893 ± 0.002	14.713 ± 0.030	16.568 ± 0.071	18.380 ± 0.277	21.392 ± 0.345	
$OLV_{1,60}$	7.559 ± 0.001	9.053 ± 0.011	9.789 ± 0.009		10.237 ± 0.010		10.871	11.616 ± 0.013	11.892 ± 0.012	14.771 ± 0.057	16.592 ± 0.050	18.274 ± 0.095	20.821 ± 0.348	
$OLV_{1,50}$	7.559 ± 0.001	9.073 ± 0.009	9.755 ± 0.009		10.243 ± 0.009		10.952 ± 0.040	11.575 ± 0.007	11.889 ± 0.019	14.600 ± 0.222	16.544 ± 0.042	18.173 ± 0.224	21.632 ± 0.461	
$OLV_{1,40}$	7.561 ± 0.010		9.796 ± 0.009		10.218 ± 0.010	10.435 ± 0.003	10.997 ± 0.022	11.570 ± 0.049	11.888 ± 0.015	14.606 ± 0.208	16.562 ± 0.032	18.284 ± 0.123		
$OLV_{1,30}$	7.560 ± 0.002	9.120 ± 0.020	9.825 ± 0.005		10.211 ± 0.001	10.440 ± 0.001	11.028 ± 0.009	11.559 ± 0.006	11.893 ± 0.001		16.494 ± 0.014	18.220 ± 0.064	21.518 ± 0.010	22.753 ± 0.004
$OLV_{1,20}$	7.560 ± 0.007		9.820 ± 0.001		10.209 ± 0.001	10.452 ± 0.005	11.037 ± 0.010	11.596 ± 0.034	11.896 ± 0.009	14.486 ± 0.076	16.507 ± 0.031	18.223 ± 0.103		
$OLV_{1,10}$	7.584 ± 0.009		9.820 ± 0.001		10.210 ± 0.006	10.456 ± 0.007	10.970 ± 0.024	11.576 ± 0.014	11.898 ± 0.019	14.638 ± 0.063	16.516 ± 0.117			
Δ (μm)	0.025	0.217	0.070	0.027	0.041	0.022	0.166	0.057	0.032	0.620	0.235	0.240	0.876	0.213
Slope	0.000	−0.003	−0.001	−0.001	0.000	−0.001	−0.001	0.000	0.000	0.007	0.002	0.003	−0.011	0.001
χ2	0.001	0.003	0.002	0.000	0.000	0.000	0.026	0.002	0.000	0.107	0.018	0.017	0.377	0.051
	Peak Position (μm) for the 45-63 μm samples													
	1	**2 (CF_1)**	**3 (sh)**	**4**	**5**	**6^+**	**7^+**	**8**	**9^+**	**10 (CF_2)**	**11^+**	**12**	**13**	**14**
$OLV_{1,100}$	7.56 ± 0.002	8.937 ± 0.022	9.766 ± 0.001	9.837 ± 0.015	10.264 ± 0.009		11.033	11.576 ± 0.001	11.845 ± 0.020	14.971 ± 0.107	16.758 ± 0.046	18.484 ± 0.099	20.917 ± 0.275	22.818 ± 0.232
$OLV_{1,90}$	7.57 ± 0.010	8.929 ± 0.015	9.736 ± 0.009	9.919 ± 0.099	10.269 ± 0.006		11.057	11.626 ± 0.001	11.885 ± 0.024	14.928 ± 0.056	16.672 ± 0.062	18.596 ± 0.1105	20.444 ± 0.130	21.788 ± 0.156
$OLV_{1,80}$	7.57 ± 0.002	8.988 ± 0.013	9.766 ± 0.001	10.052 ± 0.022	10.259 ± 0.010		10.963	11.579 ± 0.008	11.859 ± 0.020	15.035 ± 0.028	16.623 ± 0.071	18.186 ± 0.252	20.718 ± 0.089	22.785 ± 0.284
$OLV_{1,70}$	7.59 ± 0.086	9.011 ± 0.012	9.771 ± 0.008	9.911 ± 0.019	10.249 ± 0.001		10.963	11.601 ± 0.001	11.867 ± 0.001	14.867 ± 0.080	16.533 ± 0.045	18.497 ± 0.054	21.059 ± 0.380	22.990 ± 0.288
$OLV_{1,60}$	7.56 ± 0.006	9.034 ± 0.016	9.783 ± 0.001	10.070 ± 0.047	10.241 ± 0.009		10.963	11.572 ± 0.012	11.892 ± 0.001	14.913 ± 0.142	16.469 ± 0.034	17.989 ± 0.055	21.355 ± 0.383	22.835 ± 0.223
$OLV_{1,50}$	7.55 ± 0.001	9.119 ± 0.018	9.774 ± 0.015		10.250 ± 0.004		10.94	11.576 ± 0.001	11.867 ± 0.018	14.835 ± 0.138	16.460 ± 0.077	18.017 ± 0.216	20.780 ± 0.443	22.853 ± 0.268
$OLV_{1,40}$	7.55 ± 0.010	9.116 ± 0.021	9.769 ± 0.007	10.032 ± 0.041	10.227 ± 0.003		10.955 ± 0.023	11.565 ± 0.013	11.878 ± 0.013	14.634 ± 0.232	16.410 ± 0.047	18.075 ± 0.195	20.754 ± 0.399	
$OLV_{1,30}$	7.56 ± 0.007	9.128 ± 0.010	9.803 ± 0.001		10.227 ± 0.001		10.973 ± 0.058	11.552 ± 0.043	11.887 ± 0.011	14.666 ± 0.176	16.475 ± 0.112	18.177 ± 0.102		
$OLV_{1,20}$	7.55 ± 0.002	9.146 ± 0.001	9.780 ± 0.007		10.227 ± 0.001		10.962 ± 0.030	11.550 ± 0.035	11.891 ± 0.005	14.671 ± 0.129	16.558 ± 0.027	18.355 ± 0.054		
$OLV_{1,10}$	7.54 ± 0.006		9.820 ± 0.001		10.209 ± 0.001	10.454 ± 0.002	11.021 ± 0.021	11.548 ± 0.063	11.893 ± 0.005	14.776 ± 0.409	16.573 ± 0.037	18.146 ± 0.151		
Δ	0.047	0.217	0.084	0.232	0.060	N/A	0.117	0.077	0.048	0.400	0.348	0.607	0.911	1.203
Slope	0.000	−0.003	−0.001	−0.003	0.001	N/A	0.000	0.001	0.000	0.004	0.002	0.004	−0.003	−0.010
χ2	0.403	0.939	0.617	0.480	0.901	N/A	0.135	0.601	0.479	0.682	0.384	0.264	0.044	0.180

Table 3
The position of each dip feature for the OLV_1 spectral series. Asterisks (*) indicate provisional primary spectral absorptions (reststrahlen bands) when surface scattering dominates. TF stands for Transparency Feature.

	Dip Position (μm) for the 0-20 μm samples								
	1	**2***	**3**	**4***	**5**	**6**	**7 (TF)**	**8**	**9**
$OLV_{1,100}$	9.373 ± 0.007	10.107 ± 0.006		10.549 ± 0.022	10.998 ± 0.033		12.984 ± 0.041	15.666 ± 0.057	19.142 ± 0.200
$OLV_{1,90}$	9.351 ± 0.015	10.076 ± 0.011		10.556 ± 0.011	11.278 ± 0.049		13.084 ± 0.026	15.647 ± 0.220	19.100 ± 0.060
$OLV_{1,80}$	9.345 ± 0.009			10.660 ± 0.019	11.250 ± 0.009		13.038 ± 0.045	15.828 ± 0.362	18.927 ± 0.218
$OLV_{1,70}$	9.292 ± 0.011			10.534 ± 0.009	11.327 ± 0.032		13.049 ± 0.037	15.524 ± 0.177	18.051 ± 0.830
$OLV_{1,60}$	9.259 ± 0.003	10.046 ± 0.024		10.541 ± 0.009	11.294 ± 0.022		13.043 ± 0.031	15.474 ± 0.104	17.541 ± 0.850
$OLV_{1,50}$			10.362 ± 0.010	10.550 ± 0.014	11.348 ± 0.033	11.550 ± 0.056	13.040 ± 0.064	15.366 ± 0.060	17.165 ± 0.217
$OLV_{1,40}$			10.361 ± 0.010	10.539 ± 0.002	11.332 ± 0.028	11.698 ± 0.035	13.366 ± 0.137	15.306 ± 0.055	17.154 ± 0.035
$OLV_{1,30}$			10.364 ± 0.010	10.511 ± 0.022	11.284 ± 0.060	11.724 ± 0.026	13.309 ± 0.160	15.421 ± 0.089	17.137 ± 0.035
$OLV_{1,20}$			10.353 ± 0.006	10.532 ± 0.014	11.369 ± 0.129	11.758 ± 0.002	13.334 ± 0.219	15.396 ± 0.048	17.114 ± 0.040
$OLV_{1,10}$			10.351 ± 0.001	10.576 ± 0.011	11.424 ± 0.025	11.766 ± 0.016	13.625 ± 0.033	15.522 ± 0.015	17.183 ± 0.037
Δ	0.114	0.060	0.012	0.149	0.426	0.217	0.641	0.522	2.028
slope	0.003	0.001	0.000	0.000	−0.003	−0.005	−0.006	0.004	0.026
χ2	0.001	0.000	0.000	0.014	0.051	0.006	0.096	0.127	1.324
	Dip Position (μm) for the 20-45 μm samples								
	1	**2***	**3**	**4***	**5**	**6**	**7 (TF)**	**8**	**9**
$OLV_{1,100}$	9.350 ± 0.009	10.115 ± 0.009		10.530 ± 0.011	10.873 ± 0.004		12.955 ± 0.106	15.650 ± 0.030	18.865 ± 0.082
$OLV_{1,90}$	9.343 ± 0.003	10.110 ± 0.005		10.537 ± 0.008	10.939 ± 0.001		13.100 ± 0.025	15.534 ± 0.033	18.852 ± 0.096
$OLV_{1,80}$	9.335 ± 0.009	10.100 ± 0.010		10.532 ± 0.010	11.079 ± 0.043		13.160 ± 0.041	15.603 ± 0.034	18.961 ± 0.256
$OLV_{1,70}$	9.316 ± 0.009	10.083 ± 0.036		10.527 ± 0.011	11.312 ± 0.040		13.184 ± 0.104	15.601 ± 0.041	18.025 ± 0.740
$OLV_{1,60}$	9.310 ± 0.003			10.541 ± 0.007	11.305 ± 0.029		13.293 ± 0.126	15.533 ± 0.089	17.440 ± 0.533
$OLV_{1,50}$	9.302 ± 0.009			10.526 ± 0.010	11.227 ± 0.014	11.617 ± 0.048	13.183 ± 0.074	15.639 ± 0.053	17.529 ± 0.567
$OLV_{1,40}$			10.371 ± 0.004	10.527 ± 0.011	11.353 ± 0.003	11.690 ± 0.026	13.249 ± 0.043	15.489 ± 0.052	17.127 ± 0.065
$OLV_{1,30}$	9.295 ± 0.003		10.365 ± 0.001	10.528 ± 0.005	11.437 ± 0.003	11.694 ± 0.001	13.679 ± 0.001	15.104 ± 0.012	17.186 ± 0.013
$OLV_{1,20}$			10.368 ± 0.006	10.537 ± 0.007	11.410 ± 0.026	11.749 ± 0.015	13.503 ± 0.135	15.503 ± 0.041	17.204 ± 0.077
$OLV_{1,10}$			10.369 ± 0.002	10.527 ± 0.012	11.415 ± 0.019	11.734 ± 0.021	13.736 ± 0.021	15.446 ± 0.167	17.249 ± 0.037
Δ (μm)	0.048	0.033	0.006	0.015	0.563	0.133	0.780	0.546	1.834
slope	0.001	0.001	0.000	0.000	−0.006	−0.003	−0.008	0.003	0.023
χ2	0.938	0.916	0.000	0.052	0.809	0.839	0.810	0.310	0.802
	Dip Position (μm) for the 45-63 μm samples								
	1	**2***	**3**	**4***	**5**	**6**	**7**	**8**	**9**
$OLV_{1,100}$	9.360 ± 0.001	10.128 ± 0.004		10.539 ± 0.007	11.039 ± 0.017		12.924 ± 0.047	15.695 ± 0.033	18.934 ± 0.047
$OLV_{1,90}$	9.343 ± 0.004	9.964 ± 0.078		10.538 ± 0.014	11.055 ± 0.001		13.180 ± 0.038	15.596 ± 0.042	18.881 ± 0.043
$OLV_{1,80}$	9.330 ± 0.006	10.127 ± 0.001		10.538 ± 0.005	10.941 ± 0.011		13.076 ± 0.035	15.636 ± 0.027	18.895 ± 0.076
$OLV_{1,70}$	9.333 ± 0.008	10.127 ± 0.004		10.518 ± 0.001	10.939 ± 0.001		13.140 ± 0.044	15.597 ± 0.026	18.873 ± 0.306
$OLV_{1,60}$	9.327 ± 0.001	10.080 ± 0.015		10.534 ± 0.009	10.971 ± 0.057	11.707 ± 0.045	13.234 ± 0.172	15.543 ± 0.033	17.457 ± 0.159
$OLV_{1,50}$	9.331 ± 0.009			10.542 ± 0.013	10.948 ± 0.055		13.182 ± 0.065	15.449 ± 0.060	17.444 ± 0.276
$OLV_{1,40}$	9.328 ± 0.007	10.084 ± 0.013		10.518 ± 0.001	11.364 ± 0.073		13.167 ± 0.066	15.627 ± 0.039	17.338 ± 0.120
$OLV_{1,30}$	9.294 ± 0.002			10.521 ± 0.008	11.428 ± 0.048	11.593 ± 0.058	13.329 ± 0.250	15.649 ± 0.041	17.375 ± 0.108
$OLV_{1,20}$	9.322 ± 0.009			10.515 ± 0.007	11.388 ± 0.047	11.691 ± 0.089	13.488 ± 0.089	15.688 ± 0.057	17.267 ± 0.048
$OLV_{1,10}$			10.368 ± 0.009	10.562 ± 0.001	11.390 ± 0.032	11.722 ± 0.017	13.537 ± 0.112	15.533 ± 0.017	17.177 ± 0.065
Δ	0.065	0.164	N/A	0.047	0.489	0.129	0.613	0.246	1.757
slope	0.001	0.000	N/A	0.000	−0.006	0.000	−0.005	0.000	0.024
χ2	0.664	0.008	N/A	0.002	0.620	0.003	0.788	0.031	0.803

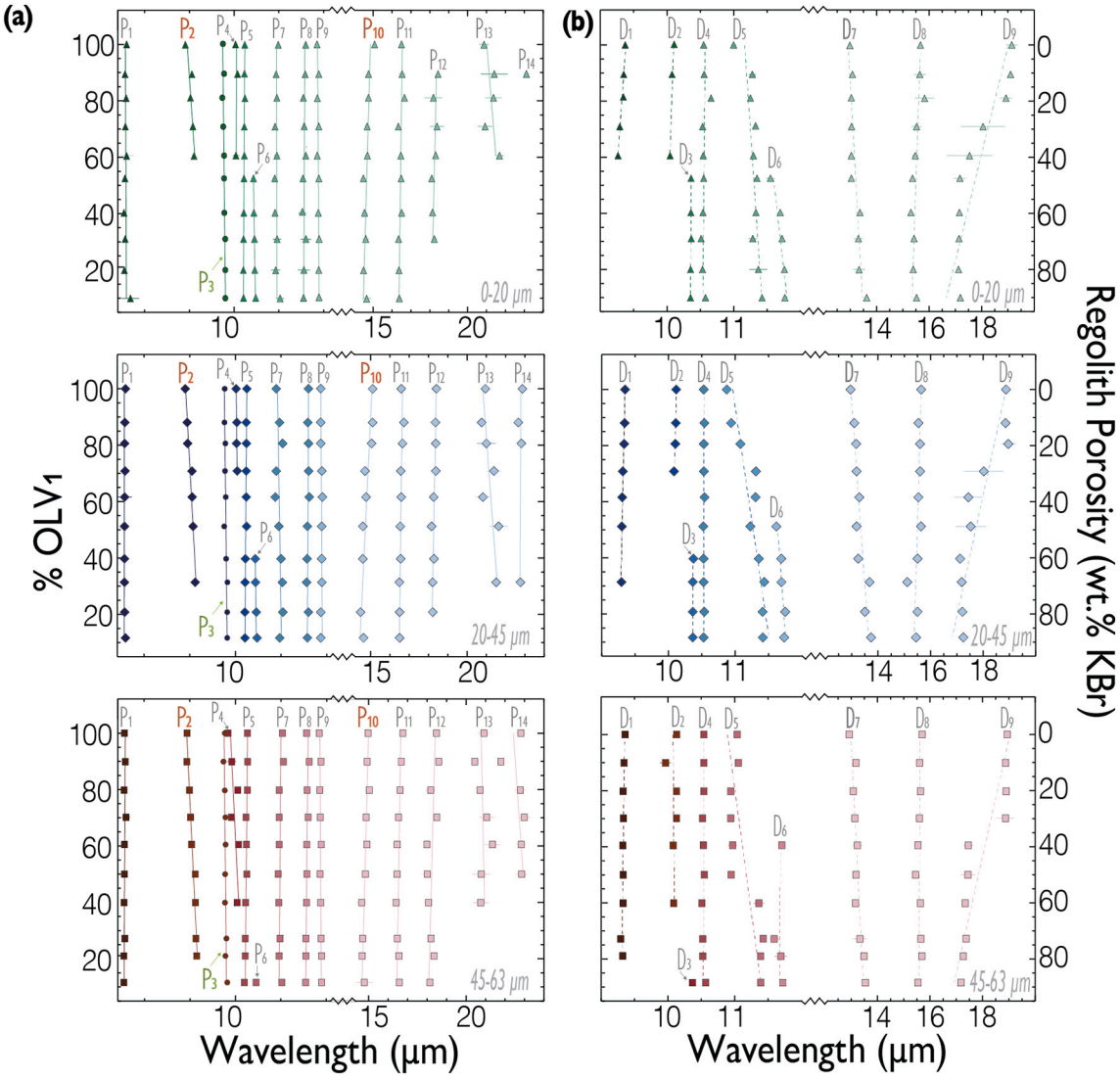

Fig. 4. Position of all defined OLV_1 (a) peaks, and (b) dips as a function of regolith porosity for particle sizes of 0–20 μm (top – green triangles), 20–45 μm (middle – blue diamonds), and 45–63 μm (bottom – red rectangles). The shoulder (P_3 - sh) is represented with circle symbols, and labeled in lime green. The two CFs (P_2 and P_{10}) are labeled in orange. The TF's (D_7) label is bolded. Gray symbols indicate weak features. Colour gradation is used to discern individual features in the 10-μm region. Note the different wavelength scales. (For interpretation of the references to colour in this figure legend, the reader is referred to the web version of this article.)

4.1.2.2. OLV_2. As with OLV_1, the band position of most peaks (Table 4) and dips (Table 5) do not depend on the regolith porosity of a given sample (Fig. 6). Two exceptions are CF_1 and CF_2. CF_1 shifts to longer wavelengths by 0.339, 0.345, and 0.150 μm, and CF_2 shifts to shorter wavelengths by 0.441, 0.543, and 0.387 μm for the 0–20 μm, 20–45 μm, and 45–63 μm spectra, respectively. As with OLV_1 spectra, the longer wavelength features, such as P_{12} that shifts 0.530 μm to longer wavelengths for the 45–63 μm spectra – possibly because the features at longer wavelengths (~ 15 μm or higher), are broad, and it is therefore difficult to consistently locate the features' centers. Unlike the CFs, typical bands used for Mg# analysis (i.e., P_4 and P_9, and the RB dips D_2 and D_4) do not shift significantly (see Section 5.2). Interestingly, the RBs, D_5 and D_6 (when regolith porosity is low), which can also be used for Mg# identification, do not shift, unlike what is found in the OLV_1 spectra. At longer wavelengths the RBs D_8 and D_9 shift to shorter wavelengths, which is consistent with the OLV_1 spectra.

The strong trends found associated with regolith porosity for the OLV_2 samples, are, much like the OLV_1 samples, spectral contrast, width, FWHM, and area of the peak and dip (see supplemental material for parameter values). As regolith porosity increases, the spectral contrast has a linear *increase* for the following features: P_1, P_6, P_7, P_9, P_{11}, P_{12} (weakly), D_3, and D_6 in each particle size studied, and a linear *decrease* for P_2, P_{10}, P_{13}, D_1, D_2, D_4, D_5 and D_7 (Fig. 7). As is the case for the OLV_1 samples, features, such as P_7, appear, while others disappear, with increasing regolith porosity. The FWHM decreases with increasing regolith porosity for P_2, P_5, P_{11}, D_4, D_5, and D_9, while the FWHM decreases for P_6, P_7, possibly P_{12} and P_{13}, D_3, D_6, D_7, and D_8. The width of P_5, P_4, P_9, P_{10}, P_{11}, D_2, D_4, D_5, D_7, and possibly D_9 decreases with increasing regolith porosity, and the width of P_6, P_7, P_{12}, D_3, and possibly D_6 and D_8, increase with increasing regolith porosity.

As was done with OLV_1, all feature parameters were explored as functions of other feature parameters (e.g., feature width vs. position), but no correlation was found with regolith porosity; more details are given in the supplementary material.

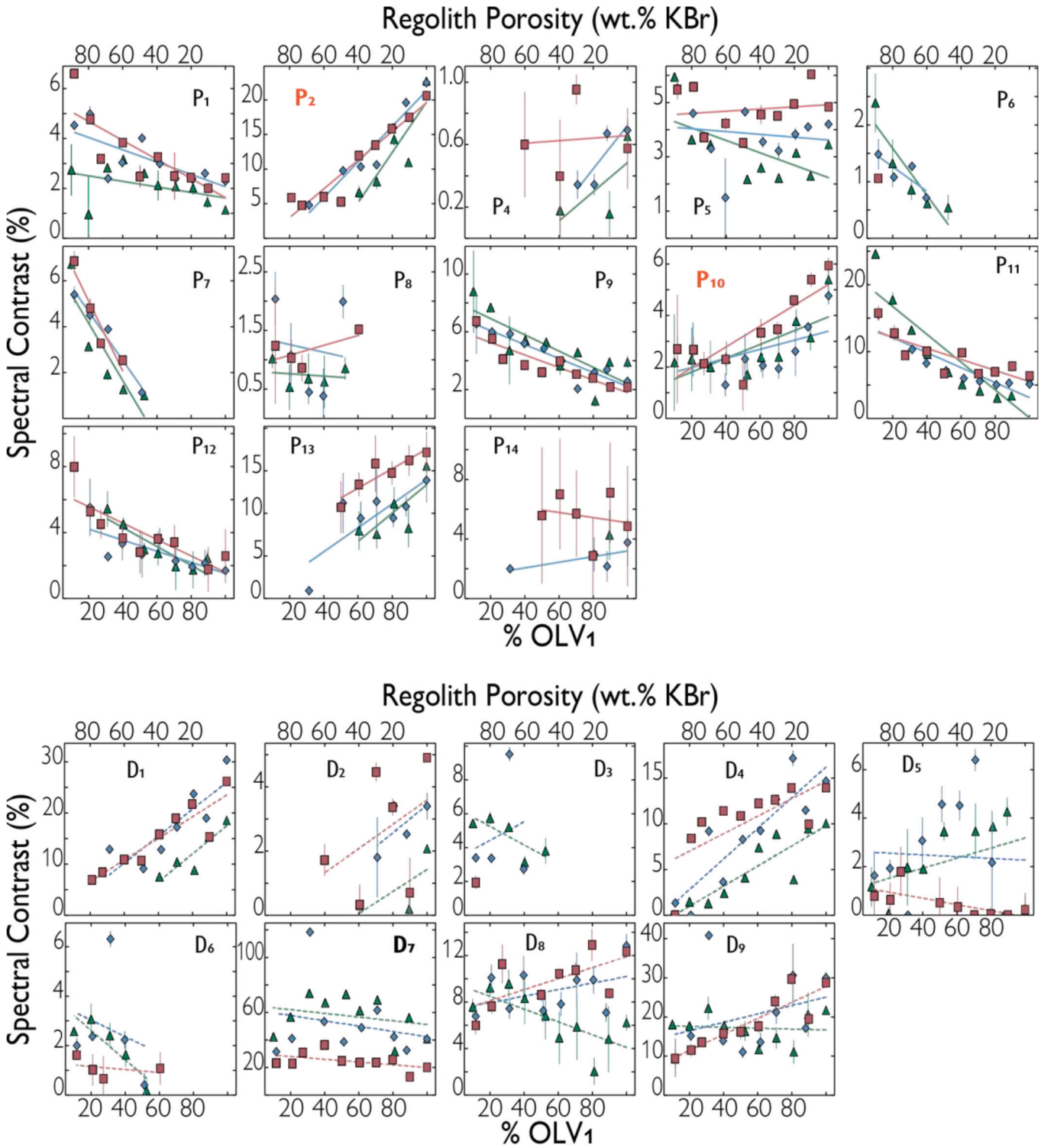

Fig. 5. Spectral contrast of OLV_1 features as a function of regolith porosity. Each panel contains a single feature in all three grain size ranges: 0–20 μm (green triangles), 20–45 μm (blue diamonds), and 45–63 μm (red rectangles). The calculated linear fit to each feature overlays the symbols. Features corresponding to *peaks* are shown on the top, and *dips* on the bottom. The CFs (P_2 and P_{10}) are labeled in orange, and the TF (D_7) is bolded. Data for all features are listed in the supplemental including fit parameters. (For interpretation of the references to colour in this figure legend, the reader is referred to the web version of this article.)

4.2. *10-μm plateau*

4.2.1. *Feature parameter definitions*

4.2.1.1. Spectra shoulder(s). A prominent character in the MIR spectra is the 10-μm plateau, defined as the positive relief emission feature that is roughly trapezoidal in shape, and spans from ~9.5 to 13 μm. We note that this designation is consistent with Emery et al. (2006), but others (e.g., Salisbury et al., 1991) use the term 'plateau' somewhat differently. The shoulder of the 10-μm plateau is defined as the short wavelength edge of the 10-μm plateau (P_3). The shoulder is a particularly important parameter to locate because other feature parameters for the overall 10-

Table 4
The position of each peak for the OLV_2 spectral series. A small plus sign (+) indicates provisional fundamental vibrational bands when volume scattering dominates.

	Peak Position (μm) for the 0-20 μm samples													
	1	**2 (CF_1)**	**3 (sh)**	**4**	**5**	**6$^+$**	**7$^+$**	**8**	**9$^+$**	**10 (CF_2)**	**11$^+$**	**12**	**13**	**14**
$OLV_{2,100}$	7.582 ± 0.030	8.880 ± 0.016	9.815 ± 0.009	9.949 ± 0.038	10.239 ± 0.003		10.980	11.640 ± 0.001	11.860 ± 0.004	15.067 ± 0.019	16.689 ± 0.022	18.479 ± 0.019	20.753 ± 0.031	
$OLV_{2,90}$	7.585 ± 0.018	8.880 ± 0.016	9.801 ± 0.008	9.960 ± 0.016	10.242 ± 0.002		10.969	11.633 ± 0.001	11.855 ± 0.005	14.997 ± 0.052	16.728 ± 0.030	18.495 ± 0.018	20.749 ± 0.010	21.894 ± 0.015
$OLV_{2,80}$	7.580 ± 0.021	8.931 ± 0.015	9.773 ± 0.018	10.016 ± 0.043	10.224 ± 0.009	10.422 ± 0.006	10.906 ± 0.146	11.601 ± 0.001	11.883 ± 0.008	14.743 ± 0.034	16.474 ± 0.004	18.374 ± 0.098	20.579 ± 0.034	
$OLV_{2,70}$	7.592 ± 0.030	9.041 ± 0.009	9.794 ± 0.001		10.215 ± 0.010	10.429 ± 0.002	10.921 ± 0.135	11.517 ± 0.068	11.878 ± 0.008	14.765 ± 0.109	16.565 ± 0.044	18.134 ± 0.131	20.696 ± 0.026	
$OLV_{2,60}$	7.586 ± 0.015	9.064 ± 0.027	9.761 ± 0.006		10.221 ± 0.002	10.429 ± 0.002	10.993 ± 0.034	11.590 ± 0.006	11.876 ± 0.007	14.626 ± 0.065	16.510 ± 0.055	18.096 ± 0.059	20.785 ± 0.008	
$OLV_{2,50}$	7.585 ± 0.011	9.045 ± 0.031	9.797 ± 0.008		10.237 ± 0.012	10.414 ± 0.014	10.904 ± 0.186	11.587 ± 0.001	11.875 ± 0.010	14.693 ± 0.070	16.500 ± 0.038	18.494 ± 0.096	20.729 ± 0.092	
$OLV_{2,40}$	7.570 ± 0.010	9.218 ± 0.029	9.803 ± 0.001		10.206 ± 0.004	10.445 ± 0.005	11.038 ± 0.019	11.549 ± 0.013	11.884 ± 0.003		16.475 ± 0.006	18.276 ± 0.037		
$OLV_{2,30}$	7.566 ± 0.014		9.782 ± 0.007		10.206 ± 0.004	10.445 ± 0.001	11.019 ± 0.013	11.549 ± 0.009	11.893 ± 0.003		16.468 ± 0.052	18.105 ± 0.081		
$OLV_{2,20}$	7.550 ± 0.009		9.793 ± 0.002		10.204 ± 0.004	10.459 ± 0.006	11.139 ± 0.020	11.588 ± 0.045	11.888 ± 0.009		16.434 ± 0.037			
$OLV_{2,10}$	7.551 ± 0.009		9.862 ± 0.001		10.199 ± 0.004	10.464 ± 0.003	11.166 ± 0.022	11.550 ± 0.034	11.890 ± 0.009		16.449 ± 0.030			
Δ	0.042	0.339	0.101	0.066	0.043	0.050	0.262	0.124	0.038	0.441	0.294	0.399	0.206	N/A
Slope	0.000	−0.005	0.000	−0.003	0.000	−0.001	−0.002	0.001	0.000	0.008	0.003	0.004	0.000	N/A
χ2	0.656	0.876	0.099	0.852	0.703	0.737	0.548	0.368	0.706	0.806	0.672	0.304	0.005	N/A
	Peak Position (μm) for the 20-45 μm samples													
	1	**2 (CF_1)**	**3 (sh)**	**4**	**5**	**6$^+$**	**7$^+$**	**8**	**9$^+$**	**10 (CF_2)**	**11$^+$**	**12**	**13**	**14**
$OLV_{2,100}$	7.608 ± 0.014	8.897 ± 0.014	9.749 ± 0.017	9.770 ± 0.042	10.279 ± 0.002		10.940			14.931 ± 0.019	16.883 ± 0.027	18.591 ± 0.122	20.634 ± 0.012	22.838 ± 0.034
$OLV_{2,90}$	7.568 ± 0.011	8.907 ± 0.011	9.739 ± 0.014	9.968 ± 0.027	10.257 ± 0.009		10.974		11.853 ± 0.005	15.058 ± 0.012	16.750 ± 0.011	18.498 ± 0.007	20.696 ± 0.032	22.847 ± 0.022
$OLV_{2,80}$	7.561 ± 0.004	8.943 ± 0.006	9.772 ± 0.009	9.981 ± 0.045	10.256 ± 0.004		10.974	11.631 ± 0.007	11.846 ± 0.011	15.041 ± 0.017	16.779 ± 0.034	18.479 ± 0.020	20.765 ± 0.055	21.832 ± 0.284
$OLV_{2,70}$	7.636 ± 0.109	8.967 ± 0.012	9.764 ± 0.012	9.900 ± 0.025	10.255 ± 0.005		10.980		11.862 ± 0.005	15.032 ± 0.035	16.626 ± 0.059	18.469 ± 0.033	20.741 ± 0.041	
$OLV_{2,60}$	7.696 ± 0.125	8.999 ± 0.010	9.766 ± 0.008	10.013 ± 0.018	10.236 ± 0.003		10.980	11.595 ± 0.024	11.880 ± 0.004	15.064 ± 0.053	16.492 ± 0.006	18.470 ± 0.037	20.662 ± 0.141	11.878 ± 0.014
$OLV_{2,50}$	7.676 ± 0.124	9.005 ± 0.021	9.772 ± 0.010	10.039 ± 0.008	10.234 ± 0.001		11.074	11.607 ± 0.010	11.882 ± 0.005	14.627 ± 0.056	16.493 ± 0.016	18.314 ± 0.149	20.820 ± 0.022	22.888 ± 0.012
$OLV_{2,40}$	7.547 ± 0.011	9.053 ± 0.027	9.781 ± 0.006	10.031 ± 0.026	10.223 ± 0.002	10.424 ± 0.005	11.243 ± 0.021	11.558 ± 0.020	11.889 ± 0.005	14.673 ± 0.181	16.447 ± 0.038	18.281 ± 0.029		
$OLV_{2,30}$	7.559 ± 0.006	9.046 ± 0.029	9.791 ± 0.004	10.040 ± 0.014	10.221 ± 0.001	10.430 ± 0.002	11.248 ± 0.035	11.546 ± 0.006	11.885 ± 0.003	14.521 ± 0.258	16.489 ± 0.014	18.169 ± 0.130		22.693 ± 0.025
$OLV_{2,20}$	7.563 ± 0.013	9.045 ± 0.036	9.803 ± 0.007	10.037 ± 0.018	10.224 ± 0.007	10.428 ± 0.007	11.241 ± 0.058	11.595 ± 0.003	11.891 ± 0.003		16.448 ± 0.034	18.365 ± 0.067		
$OLV_{2,10}$	7.564 ± 0.012	9.243 ± 0.042	9.827 ± 0.014		10.207 ± 0.002	10.449 ± 0.002	11.082 ± 0.049		11.911 ± 0.012		16.410 ± 0.012			
Δ	0.149	0.345	0.088	0.270	0.073	0.026	0.308	0.086	0.065	0.543	0.473	0.422	0.186	11.010
Slope	0.000	−0.003	−0.001	−0.003	0.001	−0.001	−0.003	0.001	−0.001	0.007	0.005	0.004	−0.002	0.025
χ2	0.067	0.806	0.861	0.606	0.927	0.715	0.622	0.461	0.882	0.598	0.848	0.717	0.394	0.022
	Peak Position (μm) for the 45-63 μm samples													
	1	**2 (CF_1)**	**3 (sh)**	**4**	**5**	**6$^+$**	**7$^+$**	**8**	**9$^+$**	**10 (CF_2)**	**11$^+$**	**12**	**13**	**14**
$OLV_{2,100}$	7.554 ± 0.024	8.894 ± 0.017	9.769 ± 0.002		10.281 ± 0.003		10.945			14.938 ± 0.031	16.892 ± 0.030	18.516 ± 0.005	20.674 ± 0.008	
$OLV_{2,90}$	7.648 ± 0.116	8.920 ± 0.016	9.742 ± 0.009	9.941 ± 0.085	10.264 ± 0.006		10.922		11.843 ± 0.011	14.871 ± 0.019	16.728 ± 0.073	18.528 ± 0.090	20.702 ± 0.031	22.877 ± 0.046
$OLV_{2,80}$	7.783 ± 0.059	8.921 ± 0.017	9.747 ± 0.004	10.005 ± 0.049	10.262 ± 0.006		10.974	11.650 ± 0.005	11.848 ± 0.007	14.847 ± 0.098	16.750 ± 0.049	18.569 ± 0.114	20.677 ± 0.003	22.827 ± 0.058
$OLV_{2,70}$	7.661 ± 0.121	8.939 ± 0.018	9.788 ± 0.005	9.966 ± 0.070	10.254 ± 0.012		10.974	11.661 ± 0.003	11.864 ± 0.011	14.949 ± 0.061	16.678 ± 0.031	18.490 ± 0.046	20.622 ± 0.061	11.839 ± 0.128
$OLV_{2,60}$	7.554 ± 0.007	8.942 ± 0.014	9.755 ± 0.007	10.008 ± 0.040	10.267 ± 0.011		10.986	11.668 ± 0.003	11.877 ± 0.012	14.847 ± 0.065	16.570 ± 0.039	18.482 ± 0.027	20.702 ± 0.004	11.843 ± 0.005
$OLV_{2,50}$	7.555 ± 0.009	8.977 ± 0.008	9.782 ± 0.011	9.975 ± 0.075	10.235 ± 0.004	10.414 ± 0.004	10.963	11.576 ± 0.020	11.890 ± 0.011	14.961 ± 0.074	16.503 ± 0.034	18.425 ± 0.082	20.713 ± 0.016	22.974 ± 0.053
$OLV_{2,40}$	7.564 ± 0.007	8.946 ± 0.024	9.770 ± 0.003	9.923 ± 0.106	10.257 ± 0.006		10.974	11.654 ± 0.001	11.874 ± 0.006	14.841 ± 0.049	16.588 ± 0.048	18.395 ± 0.184	20.662 ± 0.054	22.860 ± 0.028
$OLV_{2,30}$	7.555 ± 0.009	9.045 ± 0.017	9.835 ± 0.002	10.021 ± 0.016	10.216 ± 0.006	10.431 ± 0.003	11.032 ± 0.037	11.557 ± 0.041	11.892 ± 0.012	15.051 ± 0.071	16.439 ± 0.038	18.362 ± 0.088	21.398 ± 0.123	22.864 ± 0.017
$OLV_{2,20}$	7.591 ± 0.084	8.988 ± 0.009	9.828 ± 0.002	10.031 ± 0.012	10.210 ± 0.002	10.438 ± 0.001	11.219 ± 0.029	11.546 ± 0.016	11.893 ± 0.002	15.059 ± 0.031	16.448 ± 0.003	18.038 ± 0.029		
$OLV_{2,10}$	7.564 ± 0.019	8.963 ± 0.011	9.838 ± 0.008		10.203 ± 0.001	10.451 ± 0.003	11.159 ± 0.014		11.898 ± 0.005	14.672 ± 0.596	16.388 ± 0.013	18.093 ± 0.010		
Δ	0.229	0.150	0.096	0.108	0.078	0.036	0.297	0.122	0.056	0.387	0.504	0.530	0.776	11.136
Slope	0.001	−0.001	−0.001	−0.001	0.001	−0.001	−0.003	0.002	−0.001	0.000	0.005	0.005	−0.006	−0.038
χ2	0.176	0.581	0.682	0.170	0.817	0.986	0.655	0.584	0.855	0.002	0.909	0.753	0.320	0.022

Table 5
The position of each dip for the OLV_2 spectral series. Asterisks (*) indicate provisional primary spectral absorptions (reststrahlen bands) when surface scattering dominates. TF stands for Transparency Feature.

	Dip Position (μm) for the 0-20 μm samples								
	1	**2***	**3**	**4***	**5**	**6**	**7 (TF)**	**8**	**9**
$OLV_{2,100}$	9.346 ± 0.004	10.131 ± 0.008		10.544 ± 0.011	11.432 ± 0.040	11.781 ± 0.031	13.052 ± 0.044	15.731 ± 0.044	18.952 ± 0.026
$OLV_{2,90}$	9.358 ± 0.009	10.126 ± 0.006		10.544 ± 0.006	11.415 ± 0.010	11.730 ± 0.031	12.961 ± 0.032	15.822 ± 0.022	18.911 ± 0.016
$OLV_{2,80}$	9.335 ± 0.005	10.079 ± 0.027	10.369 ± 0.006	10.561 ± 0.020	11.398 ± 0.008	11.777 ± 0.046	12.943 ± 0.016	15.660 ± 0.051	18.910 ± 0.029
$OLV_{2,70}$	9.316 ± 0.012		10.368 ± 0.003	10.548 ± 0.011	11.388 ± 0.049	11.755 ± 0.051	12.945 ± 0.064	15.466 ± 0.087	17.185 ± 0.025
$OLV_{2,60}$	9.324 ± 0.015		10.369 ± 0.002	10.557 ± 0.012	11.365 ± 0.038	11.761 ± 0.019	12.955 ± 0.023	15.472 ± 0.035	17.147 ± 0.029
$OLV_{2,50}$	9.327 ± 0.008		10.373 ± 0.004	10.553 ± 0.020	11.372 ± 0.026	11.738 ± 0.026	12.871 ± 0.024	15.578 ± 0.061	18.948 ± 0.038
$OLV_{2,40}$	9.225 ± 0.017		10.368 ± 0.003	10.551 ± 0.017	11.423 ± 0.021	11.742 ± 0.012	13.043 ± 0.022		17.196 ± 0.041
$OLV_{2,30}$			10.362 ± 0.006	10.546 ± 0.010	11.434 ± 0.020	11.756 ± 0.006	13.051 ± 0.022		17.188 ± 0.018
$OLV_{2,20}$			10.367 ± 0.001	10.562 ± 0.015	11.430 ± 0.006	11.758 ± 0.007	13.339 ± 0.223		
$OLV_{2,10}$			10.364 ± 0.003	10.548 ± 0.003	11.437 ± 0.017	11.756 ± 0.003	13.429 ± 0.066		
Δ	0.133	0.052	0.011	0.018	0.072	0.052	0.558	0.356	1.804
Slope	0.002	0.003	0	0	0	0	−0.004	0.006	0.025
χ2	0.59	0.812	0.357	0.065	0.089	0.053	0.46	0.555	0.414
	Dip Position (μm) for the 20-45 μm samples								
	1	**2***	**3**	**4***	**5**	**6**	**7 (TF)**	**8**	**9**
$OLV_{2,100}$	9.352 ± 0.001	10.145 ± 0.002		10.531 ± 0.006			13.113 ± 0.231	15.785 ± 0.113	18.929 ± 0.165
$OLV_{2,90}$	9.337 ± 0.006	10.133 ± 0.001		10.540 ± 0.002			13.020 ± 0.054	15.731 ± 0.056	18.901 ± 0.017
$OLV_{2,80}$	9.344 ± 0.002	10.134 ± 0.004		10.540 ± 0.004	11.417 ± 0.006	11.693 ± 0.030	13.124 ± 0.061	15.718 ± 0.027	18.921 ± 0.008
$OLV_{2,70}$	9.341 ± 0.005	10.124 ± 0.040		10.539 ± 0.009			13.077 ± 0.123	15.632 ± 0.016	18.894 ± 0.030
$OLV_{2,60}$	9.327 ± 0.007	10.124 ± 0.017		10.539 ± 0.008	11.385 ± 0.008	11.731 ± 0.053	13.141 ± 0.188	15.637 ± 0.039	18.966 ± 0.049
$OLV_{2,50}$	9.319 ± 0.004	10.112 ± 0.004		10.530 ± 0.007	11.421 ± 0.009	11.741 ± 0.047	13.592 ± 0.040	15.562 ± 0.019	17.524 ± 0.041
$OLV_{2,40}$	9.303 ± 0.009	10.104 ± 0.014	10.378 ± 0.004	10.546 ± 0.011	11.442 ± 0.016	11.724 ± 0.023	13.637 ± 0.088	15.599 ± 0.031	17.411 ± 0.071
$OLV_{2,30}$	9.292 ± 0.004	10.093 ± 0.016	10.375 ± 0.001	10.544 ± 0.007	11.428 ± 0.010	11.747 ± 0.003	13.706 ± 0.050	15.514 ± 0.029	17.299 ± 0.017
$OLV_{2,20}$	9.287 ± 0.012	10.115 ± 0.005	10.375 ± 0.002	10.548 ± 0.014	11.439 ± 0.017	11.748 ± 0.028	13.679 ± 0.034		17.397 ± 0.129
$OLV_{2,10}$	9.254 ± 0.010		10.366 ± 0.001	10.555 ± 0.010			13.664 ± 0.064		
Δ	0.098	0.052	0.011	0.026	0.057	0.055	0.685	0.271	1.667
Slope	0.001	0.001	0.000	0.000	−0.001	−0.001	−0.009	0.004	0.026
χ2	0.905	0.774	0.832	0.558	0.377	0.722	0.800	0.923	0.757
	Dip Position (μm) for the 45-63 μm samples								
	1	**2***	**3**	**4***	**5**	**6**	**7 (TF)**	**8**	**9**
$OLV_{2,100}$	9.359 ± 0.006			10.530 ± 0.004			12.870 ± 0.052	15.788 ± 0.031	18.942 ± 0.001
$OLV_{2,90}$	9.349 ± 0.007	10.140 ± 0.002		10.528 ± 0.007			15.445 ± 0.773	15.707 ± 0.028	18.923 ± 0.017
$OLV_{2,80}$	9.351 ± 0.006	10.138 ± 0.007		10.544 ± 0.019	11.434 ± 0.053	11.713 ± 0.035	14.821 ± 1.249	15.703 ± 0.031	18.925 ± 0.005
$OLV_{2,70}$	9.344 ± 0.007	10.132 ± 0.025		10.535 ± 0.018	11.330 ± 0.181	11.777 ± 0.052	13.159 ± 0.164	15.662 ± 0.049	18.979 ± 0.046
$OLV_{2,60}$	9.344 ± 0.004	10.140 ± 0.003		10.524 ± 0.008	11.418 ± 0.009	11.734 ± 0.022	15.021 ± 1.009	15.662 ± 0.036	18.959 ± 0.003
$OLV_{2,50}$	9.333 ± 0.003	10.118 ± 0.048	10.378 ± 0.009	10.525 ± 0.004	11.113 ± 0.131	11.627 ± 0.047	13.561 ± 0.197	15.466 ± 0.024	17.556 ± 0.141
$OLV_{2,40}$	9.329 ± 0.047	10.083 ± 0.094		10.506 ± 0.054	11.300 ± 0.242	11.786 ± 0.040	15.183 ± 0.712	15.579 ± 0.075	18.728 ± 0.521
$OLV_{2,30}$	9.323 ± 0.004	10.124 ± 0.002	10.371 ± 0.002	10.514 ± 0.010	11.302 ± 0.168	11.743 ± 0.060	13.731 ± 0.034	15.595 ± 0.016	17.293 ± 0.036
$OLV_{2,20}$	9.326 ± 0.013	10.116 ± 0.007	10.367 ± 0.006	10.549 ± 0.006	11.430 ± 0.027	11.756 ± 0.011	13.716 ± 0.028	15.552 ± 0.015	17.239 ± 0.032
$OLV_{2,10}$	9.295 ± 0.026		10.364 ± 0.005	10.544 ± 0.005			13.782 ± 0.014	15.518 ± 0.030	17.231 ± 0.014
Δ	0.064	0.058	0.014	0.043	0.321	0.159	2.576	0.322	1.748
Slope	0.001	0.000	0.000	0.000	0.001	0.000	0.003	0.003	0.023
χ2	0.861	0.388	0.998	0.002	0.015	0.028	0.009	0.706	0.693

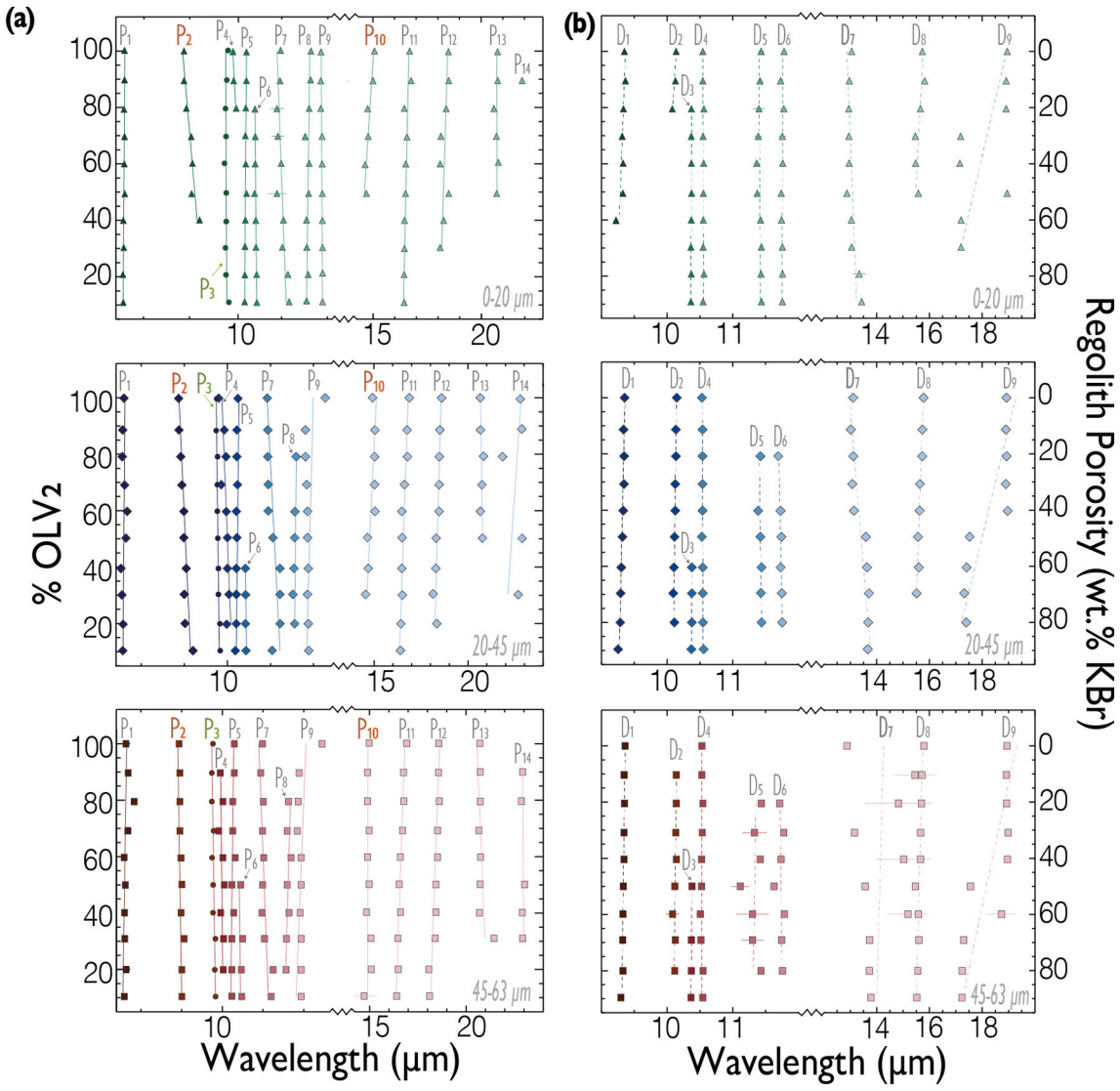

Fig. 6. Position of all defined OLV_2 (a) peaks, and (b) dips as a function of regolith porosity for particle sizes of 0–20 μm (top – green triangles), 20–45 μm (middle – blue diamonds), and 45–63 μm (bottom – red rectangles). The shoulder (P_3 - sh) is represented with circles, and labeled in lime green. The two CFs (P_2 and P_{10}) are labeled in orange. The TF's (D7) label is bolded. Gray symbols indicate weak features. Colour gradation is used to discern individual features in the 10-μm region. Note the different wavelength scales. (For interpretation of the references to colour in this figure legend, the reader is referred to the web version of this article.)

μm plateau are defined by their proximity to the shoulder, and we use the shoulder as a reference to calculate the relative height of the 10-μm plateau.

Identification of the shoulder is something of an iterative process (Fig. 8). To identify the shoulder, we begin with locating peak P_5, the prominent peak near 10.2 μm, and an inflection point (IP) around 9.5 μm as a means to bracket (or segment) the shoulder (B_1). We choose the IP for the lower bound of B_1 because it is the nearest consistent point to the short wavelength side of the shoulder, and it is not perturbed by the CF_1, regardless of particle size or porosity. Once the shoulder is bracketed, we take the second derivative of the gaussian-smoothed spectrum of this region to find where the second derivative is negative (i.e., spectrum is concave down). For a perfectly smooth spectrum, the shoulder would be defined as the most negative value in the second derivative, which marks where the change in slope reaches a minimum. Since we do not have perfectly smooth spectra, we repeat the previous step to identify a smaller spectral segment within B_1. We use the portion of the second derivative array within B_1 where values are negative to more narrowly bracket the shoulder (B_2). Then we calculate a straight line between the two positive points that define the edge of B_2 and divide B_2 by this straight line. The maximum y-value in the divided B_2 spectral segment is located and is defined as the shoulder. Error in the shoulder position is calculated in the same manner as the individual feature parameter values: by creating 10,000 synthetic spectra within the bounds of error, and repeating the above routine.

In some low porosity spectra, P_8 exhibits shoulder-like tendencies, although it appears as a clear peak in higher porosity spectra. In cases where this feature is identified as a shoulder, we quantify its location by first bracketing the search region with P_9, and an inflection point near 11 μm. Then the same shoulder routine described above is implemented.

4.2.1.2. Continua. Calculating a continuum beneath the 10-μm plateau is an important step to calculate the feature parameters. Defining a single continuum presents a challenge because the 10-μm plateau

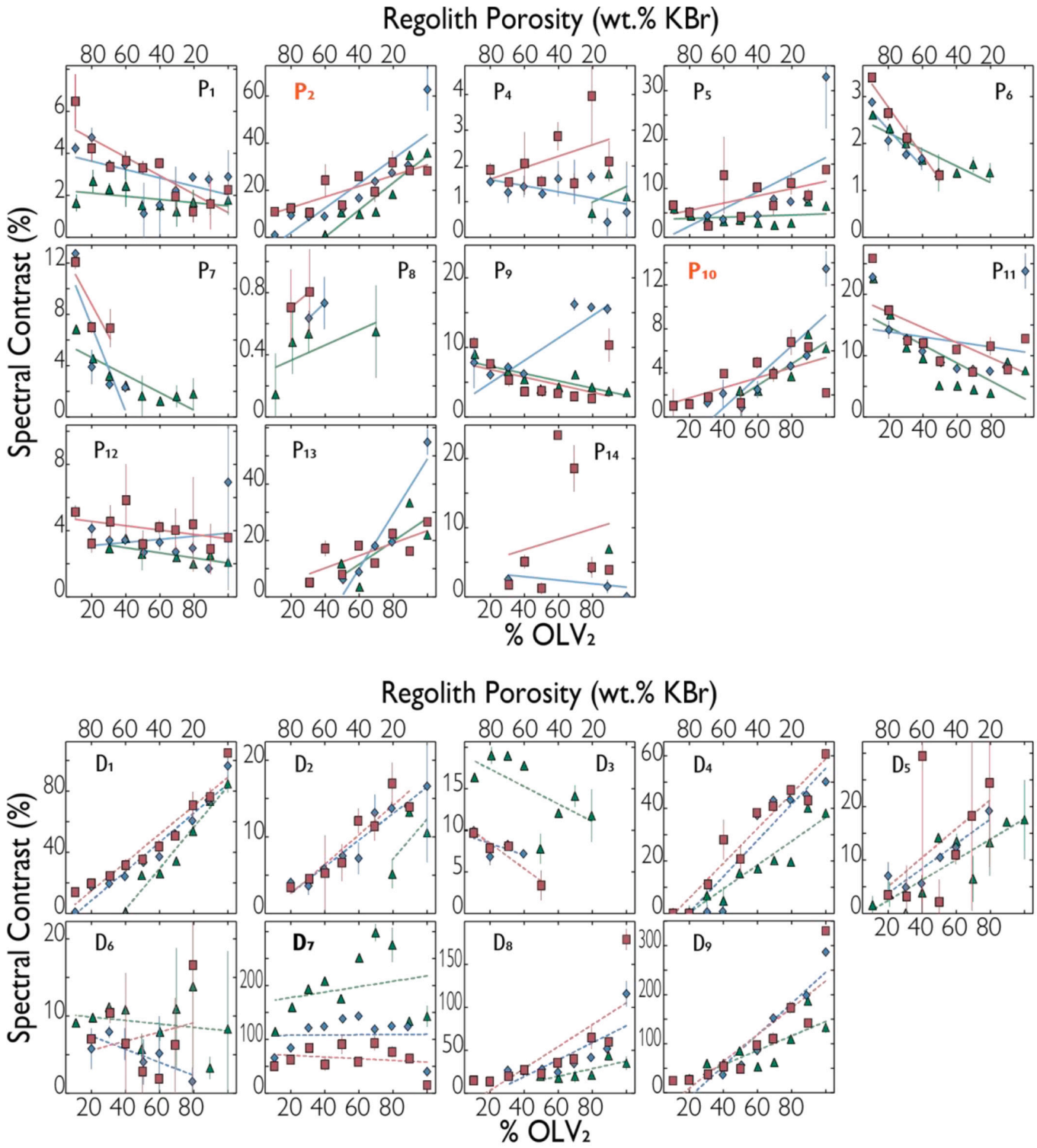

Fig. 7. Spectral contrast of OLV_2 features as a function of regolith porosity. Each panel contains a single feature in all three grain size ranges: 0–20 μm (green triangles), 20–45 μm (blue diamonds), and 45–63 μm (red rectangles). The calculated linear fit to each feature overlays the symbols. Features corresponding to *peaks* are shown on the top, and *dips* on the bottom. The CFs (P_2 and P_{10}) are labeled in orange, and the TF (D_7) is bolded. Data for all features are listed in the supplemental including fit parameters. (For interpretation of the references to colour in this figure legend, the reader is referred to the web version of this article.)

changes significantly with porosity. Thus, we define two continua, using three points ("hinges"). The 10-μm plateau is bound on the long wavelength side by a dip that roughly corresponds to a transparency feature in low porosity spectra we call the Right Hinge (RH; Fig. 9). The short wavelength side is more complicated because the CF_1 that is prominent in low-porosity spectra is absent from high-porosity spectra. Additionally, MIR spectra of Trojan asteroids and other airless bodies for which this research is applicable, have low signal to noise in the region around the CF_1 and at shorter wavelengths (e.g., Emery et al., 2006; Marchis et al., 2012). Thus, we define two hinges on the short wavelength side of the feature, so as to be useful and applicable to remote sensing spectra regardless of prior regolith porosity knowledge or ability

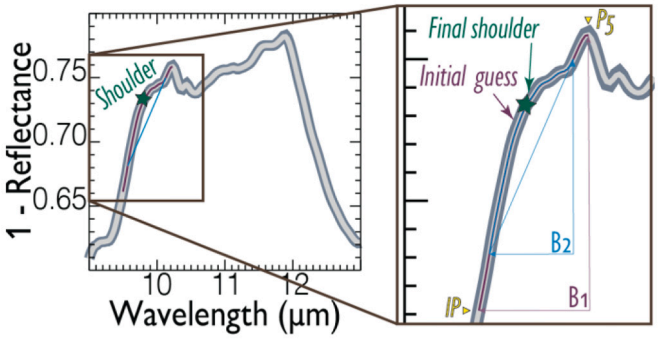

Fig. 8. Shoulder identification process, using a 0–20 μm 20% OLV_1 spectrum as an example. The calculated linear fit to each feature overlays the symbols. The zoomed in panel on the right shows the initial bracket using P_5 and the inflection point (IP) and initial bracket (B_1; maroon), and second bracket (B_2; blue) with the final shoulder pointed out (green star). (For interpretation of the references to colour in this figure legend, the reader is referred to the web version of this article.)

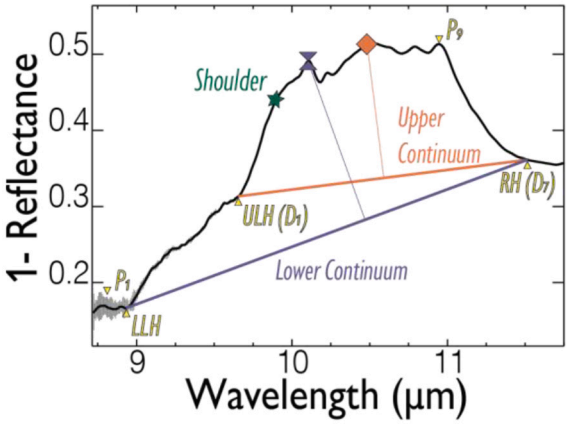

Fig. 9. Continua identification process, using a 0–20 μm 20% OLV_1 spectrum as an example. The left two Lower and Upper Left Hinge (LLH and ULH respectively), P_9, and the Right Hinge (RH) are denoted in yellow. The shoulder (green star) is also denoted. The Upper (orange), and Lower (purple) continua are represented along with the continuum-removed perpendicular line between the continuum and the band maximum (orange diamond, and purple hour glass respectively). (For interpretation of the references to colour in this figure legend, the reader is referred to the web version of this article.)

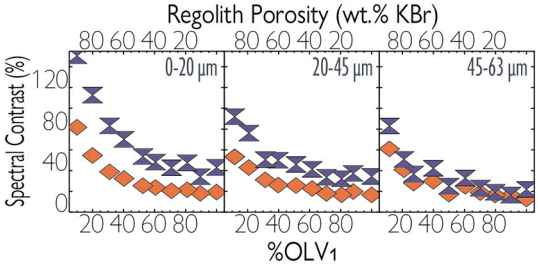

Fig. 10. Spectral contrast of the 10-μm plateau in OLV_1 as a function of $\%OLV_1$. Each panel is a different particle size bin: 0–20 μm (left), 20–45 μm (middle), and 45–63 μm (right). The Upper, and Lower continua are denoted with orange diamonds, and purple hourglasses respectively. The upper x-axis shows the corresponding regolith porosity. (For interpretation of the references to colour in this figure legend, the reader is referred to the web version of this article.)

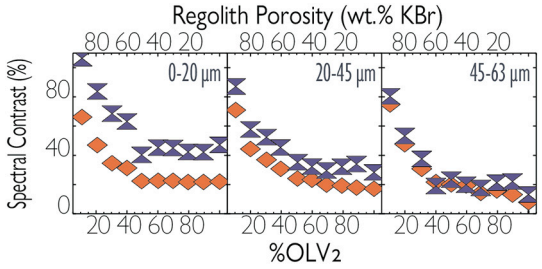

Fig. 11. Spectral contrast of the 10-μm plateau in OLV_2 as a function of $\%OLV_2$. Each panel is a different particle size bin: 0–20 μm (left), 20–45 μm (middle), and 45–63 μm (right). The Upper, and Lower continua are denoted with orange diamonds, and purple hourglasses respectively. The upper x-axis shows the corresponding regolith porosity. (For interpretation of the references to colour in this figure legend, the reader is referred to the web version of this article.)

to locate a CF_1.

The two hinges located on the left side of the broad 10-μm plateau are called Lower and Upper Left Hinge (LLH and ULH respectively). LLH is defined as the first dip in emissivity to the short-wavelength (high-frequency) side of the ν_3 bands[1] and (when surface scattering dominates) the short-wavelength side of CF_1 (P_2). The ULH is defined as the dip (D_1 at low regolith porosities) on the short-wavelength side of the ν_3 and (when surface scattering dominates) the long-wavelength of the CF_1 (P_2). For higher KBr percentages, ULH more closely resembles a small inverted shoulder, and P_2 is much smaller, or in some cases is not at all apparent. In the cases, where P_2 is not apparent, the ULH is found with the shoulder routine described above, with two differences; 1) The initial brackets are the shoulder and a point at ~9 μm, and 2) The routine looks for a concave down rather than a concave up segment. In some cases, RH is the nearest dip on the long wavelength side of P_9 (D_7), but in many cases D_7 is well into the transparency feature. In the latter case, the shoulder routine is used with P_9 and D_7 used as the initial bracketing points. The relationships between regolith porosity and the relative positions of the hinges, shoulder, and P_9 were explored for feature parameter characterization, but we did not find any relationships of note. More details can be found in the supplementary material.

To calculate the 10-μm plateau parameters (width, spectral contrast, center, skew, and slope), we first calculate continuum lines using the hinges described above (Fig. 9). We use two continuum lines: 1) the line between the LLH and the right hinge, and 2) the line between the ULH and the right hinge. Each continuum line is calculated from the end points using the IDL function '*fitexy*'. This function uses the linear least-squares approximation in one dimension and incorporates error in x and y to find the best straight-line fit. The width of the 10-μm feature is calculated by taking the difference between the right and left hinge wavelengths.

Spectral contrast and maximum value of the 10-μm plateau (band maximum) are calculated for each continuum line (Fig. 9). The following procedure is used to calculate spectral contrast, and is the same for the two continuum lines. First, the continuum removed emissivity is calculated by dividing y-values by the continuum. The center is the maximum continuum-removed y-value.

Skew is defined as the extent to which the overall 10-μm plateau leans to the left or right and is calculated from the band maximum position of the continuum removed 10-μm plateau. We compute the skew for both left hinges by finding the difference between the wavelength of the band maximum and the left hinge and dividing by the width. Values less than 0.5 skew to the right, and values greater than 0.5 skew to the left.

[1] ν_3 bands consist of three fundamental vibrational bands that result from Si—O asymmetric stretching (see Hofmeister, 1997 and Hamilton, 2010).

4.2.2. Feature parameters trends

4.2.2.1. OLV_1. The 10-μm plateau undergoes a variety of changes with increasing regolith porosity (Fig. 10). The most significant trend, which we discuss further in Section 5, is that spectral contrast decreases exponentially with decreasing regolith porosity for both continuum definitions (Fig. 10). The width also decreases slightly with decreasing porosity for the Upper continua fit but remains relatively unchanged for the Lower continua (see supplementary material). The differences in values and trends associated with the two continua highlight the necessity of measuring each of them.

The band maximum, skew and slope were not found to have significant trends with regolith porosity. In addition to analysis between feature parameters and regolith porosity, we performed analyses comparing each feature parameter to the other feature parameters and found no strong trends between the parameters. Data tables for these parameters can be found in the supplementary material.

4.2.2.2. OLV_2. The most important trend found associated with % OLV, or regolith porosity, spectral contrast and slope of the underlying continuum. With decreasing porosity, the spectral contrast decreases exponentially for each continuum definition (Fig. 11), as was observed with OLV_1. The lower continuum slope increases slightly with increasing % OLV_2, until ~30% OLV_2, at which point the slope begins to decrease. For the upper continuum fit, a slight uptick in slope occurs near ~70% OLV_2 (see supplementary material).

Similar to the OLV_1 analysis, the band maximum, skew and width were not found to have significant trends with regolith porosity. We also performed analyses comparing each feature parameter to the other feature parameters and found no strong trends between the parameters. Data tables for these parameters can be found in the supplementary material.

5. Discussion

Above we have shown that the MIR spectra of two olivine minerals of similar composition vary as a function of wt% OLV mixed with KBr, which we argue is a spectral proxy for regolith porosity. Through detailed analysis of these spectra, we have investigated whether and to what degree a number of different feature parameters are altered as the regolith porosity is varied in samples of three different particle size ranges. In Section 5.1, we focus on the feature parameters that may be the most useful for remote sensing observations: spectral contrast of the 10-μm plateau, and spectral contrast and band position of RBs, fundamental vibrational bands, and CFs. We note that our MIR spectra were measured in ambient conditions, and emission spectra are sensitive to the environment in which they are measured (e.g., Maturilli et al., 2016; Donaldson Hanna et al., 2012, 2019; Shirley and Glotch, 2019), so we compare our results to similar laboratory studies in Section 5.2, and we discuss the pertinence of our results to airless bodies and apply our results to Trojan asteroids in Sections 5.3 and 5.4.

5.1. Quantifiable effects of regolith porosity on MIR spectra

5.1.1. 10-μm plateau

The spectral contrast of the entire 10-μm plateau (~9.5 to 13 μm) relative to the defined continua exponentially increases with increasing regolith porosity for both olivine samples (Figs. 10 and 11). The increase in spectral contrast is observed for both continua in all particle sizes, but it is stronger in the smaller particle size sample. The spectral contrast of the 10-μm plateau is ~20% for regolith porosities lower than about 50%, but is significantly higher for higher porosities (spectral contrast values over 100%) All samples show similar exponential trends and values of spectral contrasts, with the exception of the <20 μm OLV_1 sample. The spectral contrast of <20 μm OLV_1 spectra at high regolith porosities is substantially higher than the other measured samples (e.g., the spectral contrast of <20 μm $OLV_{1,10}$ and 45–63 μm $OLV_{1,10}$ is 151% and 83% respectively). While there are differences in sample cup porosity (i.e., vol% of sample within the sample cup), it is not significant enough to explain the differences in spectral contrast. A possible explanation is that the particle size distribution of the <20 μm sample may skew smaller compared to the OLV_2 < 20 μm sample. A larger concentration of smaller particles would account for the overall higher spectral contrast values. Currently, we do not have the necessary equipment to make such a particle size distribution measurement, but it is reasonable to assume that since there is no lower particle size limit to this bin that more fine-particulates may be present. It may be useful for future investigations to characterize the particle size distributions.

5.1.2. Christiansen features

The CF_1 decreases in spectral contrast gradually, relative to the adjoining spectral features, with increased regolith porosity until the feature disappears entirely in the OLV_1 spectra and the <20 μm spectral suite. Similarly, P_{10}, the longer wavelength CF_2, follows a decreasing spectral contrast trend with increasing regolith porosity (Figs. 5 and 7). The rate of spectral contrast decrease is also particle size dependent. For example, CF_1 is identifiable in the spectra of 45–63 μm OLV_1 and OLV_2 for regolith porosities of 80% and 90% respectably (i.e., 20% and 10% OLV); yet disappears when the regolith porosity is 40% (OLV_1) and 60% (OLV_2) in the <20 μm samples. CFs are surface scattering features that arise when the scattering regime transitions from volume to surface scattering along the electromagnetic spectrum (Hapke, 2012), and decreasing the particle size promotes a transition into volume scattering (e.g., Salisbury and Wald, 1992; Mustard and Hays, 1997). As CFs are not features directly caused by fundamental or overtone vibrations, it is expected that their appearance is directly tied to regolith porosity in our experiments (i.e., when KBr is used as a proxy for regolith porosity).

The CF positions do shift with changing porosity. CF_1 (P_2) shifts 0.217 μm and 0.345 μm for the 20–45 μm OLV_1 and OLV_2 spectra, respectively, as the regolith porosity is changed from 0% to 90%. CF_2 (P_{10}) shifts 0.620 μm and 0.543 μm in the spectra of 20–45 μm OLV_1 and OLV_2 samples, respectively (Tables 2 and 4). The CF_1 (P_2) position has been used to determine bulk composition of airless bodies, such as the Moon (e.g., Logan and Hunt, 1970; Greenhagen et al., 2010). CF positions are known to also be sensitive to other important properties, such as particle size and thermal gradient (e.g., Hapke, 1996; Donaldson Hanna et al., 2012). For spectral analysis of a porous regolith, the 10-μm region fundamental bands are more reliable features compared to CFs for mineral identification when OLV is intimately mixed with a KBr powder.

5.1.3. Individual features in 10-μm region

As is the case for the 10-μm plateau, individual features within the region, such as P_5, P_6, and P_7 increase in spectral contrast with increasing regolith porosity. Conversely, the dips D_2, D_4, and D_5, in the same spectral region tend to decrease in spectral contrast. Both the increasing and decreasing trends are likely a result of the transition between surface scattering at low regolith porosities, to volume scattering at high regolith porosities. For the spectra dominated by surface scattering (i.e., 0% KBr), we tentatively identify D_2, and D_4, as RBs based on comparisons with RBs reported in previous work in the surface scattering regime (e.g., Hamilton, 2010 and Lane et al., 2011). For the spectra dominated by volume scattering (i.e., 90% KBr), we tentatively identify P_6, and P_7 as the ν_3 vibrational stretching bands based on comparisons with vibrational band peaks reported in previous work in the volume scattering regime (e.g., Koike et al., 2003). We do note that the spectra of the 0% regolith porosity samples (i.e., 100% OLV) may not be entirely in the surface scattering regime, as our particle sizes are low and the total simulated porosity is at least 52% (see OLV_2 45–63 μm; Table 1). Likewise, the 90% regolith porosity spectra are not exclusively volume scattering. Thus, fundamental vibrational bands may be present

in the low regolith porosity spectra, and RBs may be present in high porosity spectra (e.g., D_4). There appears to be a gradual transition to a regime where scattering is not as important and the spectrum begins to be dominated by absorption/emission at the highest regolith porosities.

One key finding of our study is that some feature positions change with regolith porosity, but many peaks and dips observed in our spectra do not shift considerably with regolith porosity. For instance, the position of some RBs in the 10-μm region, which are often used for silicate identification, are unaffected by regolith porosity, such as D_2 and D_4.

Many of the RBs lose spectral contrast with increasing regolith porosity due to scattering regime transitions, so it is prudent to note that some peaks associated with fundamental vibrational bands in the 10-μm region (e.g., P_6 and P_9) do not shift positions, and can be used for mineral identification. The peak, P_7, a likely vibrational band (discussed further below), can shift up to 0.117 μm (45–63 μm OLV_1) and 0.308 μm (20–45 μm OLV_2) as the regolith porosity is increased from 0% to 90%. Additionally, P_7 is rather tilted and shallow at low regolith porosities, making the position difficult to more quantify. Thus, the analysis of Mg# with peak position of the olivine asymmetric stretching bands is not regolith porosity dependent.

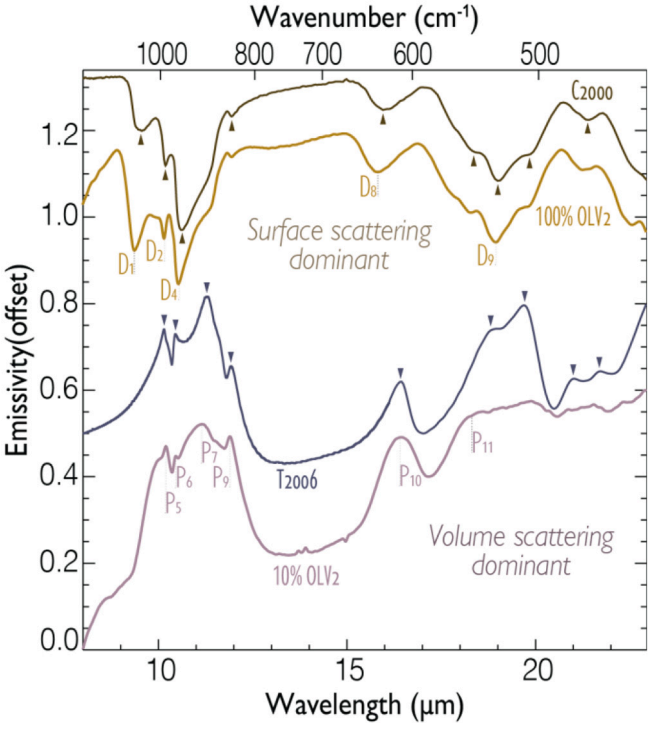

Fig. 12. Four spectra of olivine in two different scattering regimes are shown in this figure. The top spectrum (brown), labled 'C2000', is of forsteritic olivine (Christensen et al., 2000) with upward pointing arrows indicating bands defined in Hamilton (2010). The second spectrum from the top (yellow) is of the 100% OLV_2 45–63 μm sample. Dips identified in this work that correspond to C2000 bands defined are labeled. We note the similarities between the 100% OLV_2 and C2000 spectrum, such as deep RBs, and a notable CF_1. The third spectrum from the top (dark purple), labled 'T2006', is a single grain absorption spectrum of forsteritic olivine (Tamanai et al., 2006), with downward pointing arrows indicating band positions defined in Tamanai et al. (2006). The bottom spectrum is of the 10% OLV_2 0–20 μm sample. Peaks identified in this work that correspond to T2006 bands are labeled. The 10% OLV_2 and T2006 spectra both have pronounced 10-μm plateaus and deep TFs, the 10% OLV_2 spectrum is primarily in the volume scattering regime. (For interpretation of the references to colour in this figure legend, the reader is referred to the web version of this article.)

5.1.4. Individual features longward of 10-μm region

The features at longer wavelengths ($\gtrapprox$15 μm) that have been used for mineral identification (P_{11}, P_{13}, D_8, and D_9) shift with regolith porosity. These features are wider, and there is more noise in this region leading to higher uncertainties in position. The most prominent features, P_{11} and D_8, shift only slightly compared to the other features in this wavelength region. The largest shifts in the P_{11} and D_8 features are 0.564 μm (20–45 μm OLV_1) and 0.504 μm (45–63 μm OLV_2) shortward. The largest P_{13} and D_9 shifts are 2.028 μm (0–20 μm OLV_1) and 1.804 μm (0–20 μm OLV_2) shortward. Thus, the position shifting in this spectral region may not be due to the regolith porosity; rather, it may be caused by higher uncertainties.

5.1.5. P_7

The P_7 feature, located at ~11.0 μm, appears to be strongly tied to the regolith porosity. P_7 is very weak when regolith porosity is low ($\lesssim$40%; i.e., $\gtrsim$60% OLV), but becomes the most prominent feature in the 10-μm plateau when the porosity is at least 60% (depending on the particle size). An emission feature in this location is seen in the spectra of comets C/2007 N3 Lulin (Woodward et al., 2011) and 9P/Tempel 1 (Harker et al., 2005). According to their spectral modeling, this feature is identified as a fundamental forsteritic olivine feature.

As mentioned previously, we consider P_7 a ν_3 band. Koike et al. (2003) identifies a fundamental Si—O stretching feature at 11.2 μm in an absorption spectrum of San Carlos olivine. Interestingly, P_7 in <20 μm spectra of OLV_2 (San Carlos olivine) shifts ~0.26 μm from 10.91 μm at 0% regolith porosity to 11.17 μm at 90% regolith porosity, migrating closer to the feature identified in Koike et al. (2003). A possible explanation is that surface scattering is strong at low regolith porosities surface scattering is strong, and scattering features (e.g., RBs) dominate the 10-μm spectral region. As regolith porosity increases, fundamental vibrational bands (such as P_7) come to dominate the 10-μm spectral region with the transition to volume scattering. As peak values of the real and imaginary indices are at slightly different wavelengths, a slight shift occurs as the relative contributions of surface versus volume scattering change with increased regolith porosity. Thus, P_7 moves toward the actual position of the fundamental band with increased regolith porosity. Thus, the prominence, as well as the position relative to what has been measured with absorption spectroscopy, of P_7 may therefore be a strong indicator of regolith porosity.

5.1.6. P_9

Finally, our analysis suggests that if one is looking at an object with abundant surface olivine, the most stable and consistent feature to use to gain information about the Mg# is P_9 (~11.9 μm). This position does not shift with regolith porosity, and its overall appearance remains consistent over the range of studied porosities. Thus, for olivine-dominated surfaces with high degrees of regolith porosity, P_9 may be the most reliable feature for compositional characterization. For quantifiable information about the regolith structure, we can look to the overall shape of the 10-μm plateau, the visibility of the CFs, the strength of P_7, and possibly the spectral contrast of the TF. Though particle size does have an effect on the relative spectral contrast of peaks, dips, and the 10-μm plateau, the overall spectral behavior is unchanged.

5.2. Comparisons with other laboratory studies

Our findings are consistent with other studies that incorporate KBr into fine-particulate, powdered samples. Spectra of phyllosilicate samples diluted with three to four mixing ratios of KBr show shifted CFs, deeper and wider TFs, and no measurable changes in band positions as more KBr is added to the sample (Young et al., 2019). Vernazza et al. (2012) and Izawa et al. (2021) mixed KBr with powdered meteorites. Olivine rich meteorite power that had been diluted with KBr showed increased spectral contrast of the 10-μm plateau and the TF, just as we see in the spectra presented in this paper. Though Izawa et al. (2021) do

not include feature positions, their spectra of 10% Allende and 10% Leoville (CV chondrites) show a trapezoidal 10-μm plateau with high spectral contrast. However, their 50% meteorite spectra have lower spectral contrast compared to our 50% olivine spectra. This is likely due to their material being darker than our OLV samples, as Young et al. (2019) showed adding a darkening material dampens the overall spectral contrast in a KBr-diluted silicate spectrum.

Most importantly, previous studies with samples diluted in KBr show a clear difference between a dominantly surface and a dominantly volume scattering regime that we see in the work presented here. Izawa et al. (2021) show the transition between dominant scattering regimes occurs somewhere between 50 and 90% KBr, but do not look at mixtures in between those values. Thus, their resulting spectral suite shows a drastic jump from primarily surface to primarily volume scattering with increased KBr. Lizardite spectra from Young et al. (2019) show a jump from dominantly surface to dominantly volume scattering between 35% and 65% KBr, yet the scattering regime of antigorite and pure silica do not show this jump. Fig. 12 illustrates the similarities between an emissivity spectrum of forsteritic olivine from Christensen et al. (2000) and the 100% OLV_2 45–63 μm sample spectrum, and the spectral similarities between an extinction spectrum of olivine from Tamanai et al. (2006) and the 10% OLV_2 0–20 μm sample spectrum. We find similar distinct spectral differences between the dominantly surface and dominantly volume scattering regime spectra (0 and 90 wt% KBr respectively), which are consistent with previous studies. In this work, we demonstrate that the transition between the two scattering regimes is gradual, and depends on particle size.

Lane et al. (2011) used MIR spectroscopy to investigate the band positions of loose powders and pressed pellets of olivine as a function of Mg# (i.e., the amount of Mg present in the olivine crystal lattice), whereas Hamilton (2010) provides a comprehensive review of olivine MIR spectra; both studies acquired olivine spectra under ambient conditions. We find that our 100% OLV spectra agree well with powdered samples of the same Mg# in both of those studies. Given the consistency in band position and Mg# between our works and the minimal change in many peak and dip positions with changing porosity, we infer that band positions in spectra of high porosity regoliths would shift corresponding to Mg#, as they do in Lane et al. (2011) and Hamilton (2010).

Lane et al. (2011) propose the band at ~10.31 μm for Fo_{100} and ~ 10.49 μm for $Fo_{89.5}$ (their band 3) is the best individual band for identifying Mg# in olivine powders measured in diffuse reflectance, as the feature shifts ~0.74 μm from Fo_{100} to Fo_0 and ~ 0.18 μm from Fo_{100} to $Fo_{89.5}$, and the R^2 value of the band position versus Mg# was 0.96. This band correlates best to our D_4, which shifts 0.015 μm and 0.047 μm for the 20–45 μm and 45–63 μm particle sizes between the lowest and highest regolith porosity samples in the OLV_1 spectral suite. D_4 shifts ~0.07 μm for the <20 μm spectra, excluding an outlier at 80% OLV_1. The shift due to regolith porosity is much smaller shift than that caused by compositional variation, supporting the utility of this feature for identifying the Mg#. Unfortunately, this band is rather weak in the low porosity data presented here (~2.3% average; see supplementary material) as well as in Lane et al. (2011) and Hamilton (2010), and thus it may not always be as easy to detect in telescopic spectra of asteroids. Note that Lane et al. (2011) have identified an emissivity maximum at 20.58 μm (486 cm^{-1}) for Fo_{100} that shifts more than any individual band, as the olivine composition goes from forsterite to fayalite. This effect is observed in both powdered and pressed-pellet synthetic olivine samples, regardless of whether they were measured in thermal emission, specular reflectance, diffuse reflectance, or attenuated total reflectance. We call the feature at this position P_{13}; however, it is not present in our spectra when regolith porosity is $\gtrsim$60%.

5.3. Environmental effects on emissivity spectra

MIR spectra are highly sensitive to environmental conditions (temperature, temperature gradient in the sample and air/vacuum pressure) in which they are measured (e.g., Maturilli et al., 2016; Donaldson Hanna et al., 2012, 2019; Shirley and Glotch, 2019). As the OLV spectra presented here were taken under ambient Earth conditions, we must be cautious with the application of our results to airless bodies. Environmental effects are due to a combination of thermal gradients in the top ~mm of the surface and wavelength-dependent scattering properties of the mineral or rock (Henderson and Jakosky, 1997). Photons emitted with frequencies near the CF often arise from deeper below the surface than those emitted near RBs because the photons are not absorbed (low absorption coefficient). Thus, in the presence of a strong thermal gradient, temperatures at the depth of CF photon emission can be more than 100 K higher than temperatures at the depth of the RB photon emission. A strong thermal gradient arises in surface materials for which the deposition of solar photons is deeper than the cooling in the MIR (e.g., quartz, olivine), an effect which is also particle size dependent (Henderson and Jakosky, 1997). Thermal gradients are reduced in objects with lower surface temperatures, such as those that are farther from the Sun (Henderson and Jakosky, 1997; Young et al., 2019). Surfaces that contain a significant fraction of opaque materials, for example, do not have such an imbalance in the depth of heating and cooling, so these vacuum spectral effects are reduced or not observed (e.g., Donaldson Hanna et al., 2019; Bates et al., 2021).

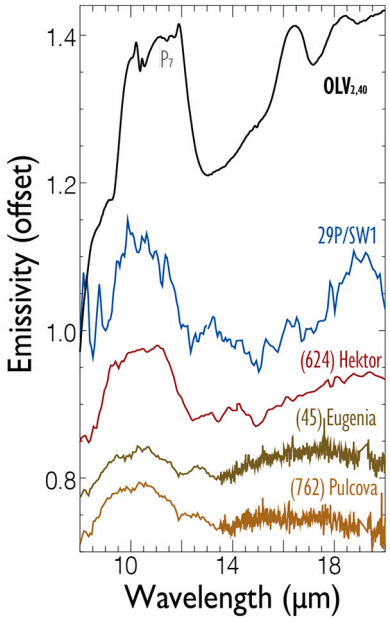

Fig. 13. Emissivity spectra of: $OLV_{2,40}$, which corresponds to 60% regolith porosity (black), comet 29P/Schwassmann-Wachmann (29P/SW1; blue), Trojan asteroid Hektor (red), asteroid Eugenia (brown), and asteroid Pulcova (dark orange). Comet and asteroid spectra are from Emery et al. (2006) and Marchis et al. (2012). (For interpretation of the references to colour in this figure legend, the reader is referred to the web version of this article.)

Pure scattering features, like CFs, change in position due to differences in both environment and porosity. Thus, it is not possible to disentangle the environmental, porosity, and compositional effects from the CF position alone. Importantly, we show that there are features whose position does not depend on environmental conditions or regolith porosity, suggesting that they can be used for mineral identification. For instance, P_9 can be used for spectral analysis of highly porous regoliths of OLV, and P_7, which is only associated with regolith porosity, can be used as a marker of regolith porosity. Even taking these potential complications dealing with the laboratory environment into account, there are ample features in our laboratory spectra that can be used for qualitative analyses of existing telescopic spectra of asteroids (like Trojan asteroids).

5.4. Applications to Trojan asteroids and other small bodies

The large spectral contrast of the 10-μm plateau with respect to both defined continua seen in our most highly porous samples is consistent with the spectra of comets and Trojan asteroid surfaces (e.g., Emery et al., 2006; Mueller et al., 2010) and is likely due to volume scattering becoming more dominant as the porosity increases. Comet comae are optically thin and show spectral contrasts of nearly 100% in some cases, whereas Hektor's 10- μm region spectral contrast is closer to 15% (Emery et al., 2006). Notably, Hektor does not have a CF_1, indicating that the spectrum is primarily in the volume scattering regime. Additionally, Trojan asteroid (617) Patroclus shows a spectral contrast of ~4% (Mueller et al., 2010), and also does not have a CF_1. From the spectra we presented here, we see that OLV tends to lose CF_1 when regolith porosity is 40 to 80% depending on particle size for OLV_1, and ~60% for the <20 μm OLV_2 spectral suite. Though the spectral contrast of both Hektor and Patroclus is much lower than any of the OLV spectra we present here, we note that their surfaces have extremely low albedos (~4%), which suggests a high abundance of darkening material, which significantly reduces the spectral contrast. It is worth reiterating that regolith porosity, as defined here, is the weight percentage of KBr in a given sample (see Section 2.2). The 45–63 μm OLV_1 80% regolith porosity sample has a *total* simulated porosity of ~92%, as it includes 80 wt% KBr plus additional void space (see Table 1). For the <20 μm OLV_1 40% regolith porosity sample, the total simulated porosity is ~81%. Spectra of < 20 μm OLV_2 samples lose their CF_1 around 60% regolith porosity, which has ~ 89% total simulated porosity. Thus, a more realistic estimation is that the surfaces of both Hektor and Patroclus are dominated by void space, or transparent material, in excess of ~81–92% by volume.

In addition to Trojans, there are other objects whose spectra may indicate porous regoliths of fine-particulate silicates. Spitzer Space Telescope spectra of asteroids (45) Eugenia and (762) Pulcova, among other main belt asteroids, have a 10-μm plateau like the Trojan asteroids, with a spectral contrast similar to the spectrum of Patroclus (Marchis et al., 2012). Qualitatively, the spectra of these objects look similar to each other as well as the high OLV_2 regolith porosity spectra presented here (Fig. 13). Each has a 10-μm plateau in the same region and are of a similar width as the OLV_2 spectrum. Hektor, and possibly SW1, Eugenia, and Pulcova all have a P_7 feature, potentially indicative of high porosity regoliths. Unfortunately, P_7 is subtle for low regolith porosity (≲40%), so the sensitivity is insufficient to determine regolith porosity in that case.

Other spectral differences between these objects may also be related to the composition. For example, Hektor is D-type while Pulcova and Eugenia are C-types. The lower spectral contrast of Pulcova and Eugenia relative to Hektor, and all three objects relative to our OLV samples may be, in part, due to differing abundances of material that reduces the spectral contrast of features in the MIR, such as amorphous carbon. The rounded shape of Eugenia and Pulcova could be caused by a larger abundance of amorphous or hydrated silicates, which both have rounded 10-μm plateaus, mixed with olivine. Judging from the presence of the P_7 feature, the relatively low spectral contrast and presence of a 10-μm plateau, it seems likely that all of these objects have porous surfaces made of fine-particulate silicates mixed with opaque minerals, with the possible addition of amorphous material. More work is needed to quantitatively assess the porosities of these surfaces.

Finally, we point out that while the variations in the MIR can be quite complex, we show that this spectral region can also enable a more detailed analysis of silicate mineralogy, as well as particle size and regolith porosity. Thus, this spectral region could serve as an important complement in asteroid taxonomy studies, which have historically relied on VNIR spectroscopy (e.g., DeMeo et al., 2009). In some cases, such as for taxonomic classes that are featureless in the NIR (e.g., D-, C-, P-type asteroids), MIR spectral analysis, such as this, will be advantageous, particularly once environmental effects at high porosity are more fully investigated.

6. Conclusions and future work

In an effort to understand the surface properties of planetary bodies, we have conducted a series of laboratory experiments with olivine of different particle sizes. MIR spectra can be difficult to interpret because of the intertwined effects of composition, particle size, and porosity. The complications in interpretation are balanced by the prospect of retrieving information about all these properties of planetary surfaces that provide an in-depth remote sensing investigation. The MIR is quite useful for a myriad of analysis due to the complexity of entwined variables such as composition, texture, and temperature.

Our results elucidate the quantifiable effect of porosity on MIR spectra in fine-particulate silicate regoliths. Overall, there is a systematic change in the CFs, as well as the 10-μm plateau as regolith porosity is increased: the primary CF decreases in spectral contrast with increasing porosity until it disappears at a porosity of 40 to 80% regolith porosity for OLV_1, whereas the 10-μm plateau increases in spectral contrast with increasing porosity. Additionally, we identified a feature (P_7) that only occurs when a regolith porosity threshold of at least ~40% regolith porosity has been surpassed. These characteristic parameters provide the means for quantifying forsterite-rich regolith porosity of distant, low-albedo, airless, bodies.

The most stable feature (i.e., changes the least with changing regolith porosity) that we identify is P_9, and thus it should be useful for mineralogical as well as compositional characterization, regardless of the regolith porosity. The band centers of other features in the 10-μm region also remain stable (e.g., D_2, D_4, P_4, and P_5), though there is a larger change in spectral contrast compared to P_9, and some features (e.g., P_4) disappear entirely with increased regolith porosity.

Utilizing MIR spectra of asteroid surfaces to infer silicate mineralogy and porosity is complementary to observations at other wavelengths, especially for spectrally featureless asteroids in the NIR such as Hektor, Pulcova, and Eugenia. Thus, when spectra are available, a more holistic approach of VNIR+MIR spectral analysis strengthens compositional assessments, as well as regolith porosity and silicate particle size determination.

Finally, here we show that the regolith porosity can clearly affect the shape and subsequent interpretation of MIR spectra of olivine-rich surfaces. However, we recognize that although olivine is a common mineral found on many extraterrestrial surfaces, it is unlikely for a surface to be comprised entirely of olivine. Thus, in future studies, we plan to explore how the porosity affects the MIR spectra of pyroxenes, phyllosilicates, and mixtures of these minerals.

Declaration of Competing Interest

None.

Acknowledgments

The authors would like to thank Sean Lindsay, Daniel Britt, Will Grundy, and Carey Lisse for invaluable discussions regarding the inception, and methodology of this work. We would also like to thank Annette Engel for the use of the spectrometer, as well as Molly McCanta and Allan Patchen for their guidance with electron microprobe sample preparation, and data acquisition at The University of Tennessee. Finally, we thank our referees (Melissa Lane and an anonymous reviewer) for their constructive reviews that significantly improved the paper. This work is supported by the National Aeronautics and Space Administration's Science Mission Directorate Research and Analysis Solar System Workings program NH19ZDA001N.

Appendix A. Supplementary data

Supplementary data to this article can be found online at https://doi.org/10.1016/j.icarus.2022.114921.

References

Bates, H.C., et al., 2021. A spectral investigation of aqueously and thermally altered CM, CM An, and CY chondrites under simulated asteroid conditions for comparison with OSIRIS- Rex and Hayabusa2 observations. JGR Planets 126.

Chihara, H., et al., 2002. Compositional dependence of infrared absorption spectra of crystalline silicates. Astron. Astrophys. 391 (1), 267–273.

Christensen, P.R., et al., 2000. Identification of a basaltic component on the Martian surface from Thermal Emission Spectrometer data. J. Geophys. Res. 105 (E4), 9609–9621.

Clark, R.N., Roush, T.L., 1984. Reflectance spectroscopy: quantitative analysis techniques for remote sensing applications. J. Geophys. Res. 89, 6329–6340.

DeMeo, F.E., et al., 2009. An extension of the Bus asteroid taxonomy into the near-infrared. Icarus 202, 160–180.

Donaldson Hanna, K.L., et al., 2012. Laboratory emissivity measurements of the plagioclase solid solution series under varying environmental conditions. J. Geophys. Res. 117, E11004.

Donaldson Hanna, K.L., et al., 2019. Spectral characterization of analog samples in anticipation of OSIRIS-REx's arrival at Bennu: a blind test study. Icarus. 319, 701–723.

Donaldson-Hanna, K.L., et al., 2017. Effects of varying environmental conditions on emissivity spectra of bulk lunar soils: application to diviner thermal infrared observations of the Moon. Icarus 283, 326–342.

Emery, J.P., Brown, R.H., 2004. The surface composition of Trojan asteroids: constraints set by scattering theory. Icarus 170 (1), 131–152.

Emery, J.P., et al., 2006. Thermal emission spectroscopy (5.2-38 μm) of three Trojan asteroids with the Spitzer Space Telescope: detection of fine-grained silicates. Icarus 182 (2), 496–512.

Fernández, Y.R., et al., 2003. The albedo distribution of jovian trojan asteroids. Astron. J. 126 (3 1773), 1563–1574.

Gail, H.P., 2004. Radial mixing in protoplanetary accretion disks - IV. Metamorphosis of the silicate dust complex. Astron. Astrophys. 413 (2), 571–591.

Greenhagen, B.T., et al., 2010. Global silicate mineralogy of the Moon from the diviner lunar radiometer. Science 329 (5998), 1507–1509.

Hamilton, V.E., 2000. Thermal infrared emission spectroscopy of the pyroxene mineral series. J. Geophys. Res. 105 (B4), 9701–9716.

Hamilton, V.E., 2010. Thermal infrared (vibrational) spectroscopy of mg-fe olivines: a review and applications to determining the composition of planetary surfaces. Chem. Erde 70 (1), 7–33.

Hamilton, V.E., et al., 2008. Visible, near-infrared, and middle infrared spectroscopy of altered basaltic tephras: spectral signatures of phyllosilicates, sulfates, and other aqueous alteration products with application to the mineralogy of the Columbia Hills of Gusev Crater, Mars. J. Geophys. Res. 113 (E12S43).

Hapke, B., 1996. Applications of an energy transfer model to three problems in planetary regoliths' the solid-state greenhouse, thermal beaming, and emittance spectra. J. Geophys. Res. 101 (E7), 16,833–16,840.

Hapke, B., 2012. Theory of Reflectance and Emittance Spectroscopy, 2nd. Cambridge University Press (ISBN 978-0521-88349-8).

Harker, D., et al., 2002. HGrain properties of comet C/1995 O1 (Hale-Bopp). Astron. J. 580, 579–597.

Harker, D., et al., 2005. The dust from 9P/Templ 1 before and after the encounter with deep impact. Science 310 (5746), 278–280.

Henderson, B.G., Jakosky, B.M., 1997. Near-surface thermal gradients and mid-IR emission spectra: a new model including scattering and application to real data. J. Geophys. Res. 102 (E3), 6567–6580.

Henning, T., 2010. Cosmic silicates. Ann. Rev. Astron. Astrophys. 48 (1), 21–46.

Hofmeister, A.M., 1997. Infrared reflectance spectra of fayalite, and absorption data from assorted olivines, including pressure and isotope effects. Phys. Chem. Miner. 24, 535–546.

Hofmeister, A.M., Pitman, K.M., 2007. Evidence for kinks in structural and thermodynamic properties across the forsterite–fayalite binary from thin-film IR absorption spectra. Phys. Chem. Miner. 34, 319–333.

Hunt, G.R., Logan, L.M., 1972. Variation of single particle mid-infrared emission spectrum with particle size. Appl. Opt. 11, 142–147.

Izawa, M.R.M., et al., 2021. Salt – a critical material to consider when exploring the solar system. Icarus 359, 114238.

Kelley, M.S., et al., 2017. Mid-infraed spectra of comet nuclei. Icarus 284, 344–358.

King, P.L., et al., 2011. Salt – a critical material to consider when exploring the solar system. In: 42nd Lunar and Planetary Science Conference (2011), Houston TX, p. 1985.

Koike, C., et al., 2003. Compositional dependence of infrared absorption spectra of crystalline silicate. Astron. Astrophys. 399 (3), 1101–1107.

Koike, C., et al., 2010. Effects of forsterite grain shape on infrared spectra. Astrophys. J. 709 (2), 983–992.

Lane, M.D., 1999. Midinfrared optical constants of calcite and their relationship to particle size effects in thermal emission spectra of granular calcite. JGR Planets 104 (E6), 14099–14108.

Lane, M.D., Christensen, P.R., 1998. Thermal infrared emission spectroscopy of salt minerals predicted for Mars. Icarus 135 (2), 528–536.

Lane, M.D., et al., 2011. Midinfrared spectroscopy of synthetic olivines: thermal emission, specular and diffuse reflectance, and attenuated total reflectance studies of forsterite to fayalite. J. Geophys. Res. 116 (8), 1–20.

Lisse, C.M., et al., 2006. Comparison of the composition of the Tempel 1 ejecta to the dust in comet C/Hale–Bopp 1995 O1 and YSO HD 100546. Icarus 187, 69–86.

Logan, L.M., Hunt, G.R., 1970. Infrared emission spectra: enhancement of diagnostic features by the lunar environment. Science 169 (3948), 865–866.

Logan, L.M., et al., 1973. Compositional implications of Christiansen frequency maximums for infrared remote sensing applications. J. Geophys. Res. 78 (23), 4983–5003.

Marchis, F., et al., 2012. Multiple asteroid systems: dimensions and thermal properties from Spitzer space telescope and ground-based observations. Icarus 221, 1130–1161.

Maturilli, A., et al., 2016. Characterization of asteroid analogues by means of emission and reflectance spectroscopy in the 1- to 100-μm spectral range. Earth Planets Space 68 (113).

Moersch, J.E., Christensen, P.R., 1995. Thermal emission from particulate surfaces: a comparison of scattering models with measured spectra. J. Geophys. Res. 100 (E4), 7465–7477.

Mueller, M., F., et al., 2010. Eclipsing binary trojan asteroid patroclus: thermal inertia from spitzer observations. Icarus 205 (2), 505–515.

Mustard, J.F., Hays, J.E., 1997. Effects of hyperfine particles on reflectance spectra from 0.3 to 25 μm. Icarus 125 (1), 145–163.

Salisbury, J.W., Wald, A., 1992. The role of volume scattering in reducing spectral contrast of Reststrahlen bands in spectra of powdered minerals. Icarus 96, 121–128.

Salisbury, J.W., Walter, L.S., 1989. Thermal infrared (2.5-13.5 μm) spectroscopic remote sensing of igneous rock types on particulate planetary surfaces. J. Geophys. Res. 94 (7), 9192–9202.

Perna, D., et al., 2018. Rotationally resolved spectroscopy of jupiter trojans (624) hektor and (911) agamemnon. Mon. Notices Royal Astron. Soc. 475 (1), 974–980.

Salisbury, J.W., et al., 1991. Midinfrared (2.5-13.5 μm) reflectance spectra of powdered stony meteorites. Icarus 92, 280–297.

Salisbury, J.W., et al., 1994. Thermal-infrared remote sensing and kirchhoff's law 1. Laboratory measurements. J. Geophys. Res. 99 (B6), 11,897–11,911.

Sharkey, B.N.L., et al., 2019. Compositional constraints for Lucy Mission Trojan asteroids via near-infrared spectroscopy. Astron. J. 158 (5), 204.

Shirley, K.A., Glotch, T.D., 2019. Particle size effects on mid-infrared spectra of lunar analog minerals in a simulated lunar environment. JGR Planets 124, 970–988.

Spitzer, W.G., Kleinman, D.A., 1961. Infrared lattice bands of quartz. Phys. Rev. 121 (5), 1324–1335.

Tamanai, A, et al., 2006. The 10 μm infrared band of silicate dust: A laboratory study comparing the aerosol and KBr pellet techniques. Astrophys. J. 648 (2), L147–L150.

Vernazza, P., et al., 2012. High surface porosity as the origin of emissivity features in asteroid spectra. Icarus 221 (2), 1162–1172.

Vernazza, P., et al., 2015. Interplanetary dust particles as samples of icy asteroids. Astrophys. J. 806 (204), 1–10.

Vincent, R.K., Hunt, G.R., 1968. Infrared reflectance from mat surfaces. Appl. Opt. 7 (1), 53–59.

Wooden, D.H., et al., 2017. Cometary dust: the diversity of primitive refractory grains. Phil. Trans. R. Soc. A 375, 20160260.

Woodward, C.E., et al., 2011. Dust in Comet C/2007 N3 (Lulin). Astron. J. 141 (181) (9 pp.).

Yang, B., Jewitt, D., 2011. A near-infrared search for silicates in Jovian Trojan asteroids. Astron. J. 141 (3), 95.

Yang, B., et al., 2013. Are large Trojan asteroids salty? An observational, theoretical, and experimental study. Icarus 223 (1), 359–366.

Young, C.L., et al., 2019. The mid-IR spectral effects of darkening agents and porosity on the silicate surface features of airless bodies. Icarus 321, 71–81.